AD NUMBER

AD405918

NEW LIMITATION CHANGE

TO
Approved for public release, distribution
unlimited

FROM
Distribution authorized to U.S. Gov't.
agencies and their contractors;
Administrative/Operational Use; APR 1963.
Other requests shall be referred to Air
Force Aeronautical Systems Division,
Materials and Processes Directorate,
Wright-Patterson AFB, OH 45433.

AUTHORITY

AFML ltr, 15 Jan 1973

UNCLASSIFIED

AD 405 918

DEFENSE DOCUMENTATION CENTER

FOR

SCIENTIFIC AND TECHNICAL INFORMATION

CAMERON STATION, ALEXANDRIA, VIRGINIA

UNCLASSIFIED

ASD-TDR-62-1064

THE RELATIONSHIP OF MICROSTRUCTURE TO STRENGTH AND TOUGHNESS IN HIGH STRENGTH STEEL

NOTICES

When Government drawings, specifications, or other data are used for any purpose other than in connection with a definitely related Government procurement operation, the United States Government thereby incurs no responsibility nor any obligation whatsoever; and the fact that the Government may have formulated, furnished, or in any way supplied the said drawings, specifications, or other data, is not to be regarded by implication or otherwise as in any manner licensing the holder or any other person or corporation, or conveying any rights or permission to manufacture, use, or sell any patented invention that may in any way be related thereto.

ASTIA release to OTS not authorized.

Qualified requesters may obtain copies of this report from the Armed Services Technical Information Agency, (ASTIA), Arlington Hall Station, Arlington 12, Virginia.

Copies of this report should not be returned to the Aeronautical Systems Division unless return is required by security considerations, contractual obligations, or notice on a specific document.

D

FOREWORD

This report was prepared by The Ohio State University Research Foundation under USAF Contract No. AF 33(616)-7780. This contract was initiated under Project No. 7351, "Metallic Materials," Task No. 735105, "High Strength Metallic Materials." The work was administered under the direction of the Directorate of Materials and Processes, Deputy for Technology, Aeronautical Systems Division, with Mr. P. L. Hendricks acting as project engineer.

This report covers work conducted from 1 April 1961 to 30 September 1962.

The torsion testing apparatus was built under the direction of Neal E. Farrar, Technical Assistant, Department of Metallurgical Engineering. Joseph D. Cox assisted in obtaining data as a student assistant.

ABSTRACT

This research deals with the relationship between the microstructural features and the susceptibility to brittle fracture of six selected commercially produced ultra-high strength steels. The parameters selected for the susceptibility to brittle fracture were the susceptibility to plastic instability, indicative of the susceptibility to ductile fracture initiation, and controlled total available energy bend test to determine the conditions for acceleration of crack propagation and the energy absorbed in rapid crack propagation. The microstructures were studied by standard techniques of optical microscopy, electron microscopy, and electron diffraction.

The true stress-true strain tensile tests of the experimental steels showed, in general, a low strain-hardening coefficient (n values of 0.04 to 0.08) and a rapid loss of capacity for strain hardening early in the plastic range. The strain at load instability in the tensile test showed no discernible correlation with the strain in torsion at the onset of structural instability in the torsion test. The experimental steels showed considerable variation in susceptibility to plastic instability, with H-11 and 300-M being outstanding in this regard. The susceptibility to plastic instability decreases as the tensile strength level is dropped from 275,000 psi to 250,000 psi.

Only preliminary results have been obtained on the controlled available energy bend test. It shows promise in being able to ferret out the important parameter that controls the acceleration of crack propagation to the running stage. There seems to be no important variation in energy absorption during the running stage.

The microstructural examination of the structures of the experimental steels showed similarities and divergences in detail. AISI 4340, D6, and D6AC have coarser carbides than 300M and MX-2; D6 and D6AC also contain undissolved carbides. All have certain common features such as platelet precipitates, parallel plate colonies, and areas of ferrite bare of carbides. The phenomenon of $500°F$ embrittlement may play a role in the nature of the mechanical response of these steels.

This technical documentary report has been reviewed and is approved.

I. Perlmutter

Chief, Physical Metallurgy Branch
Metals and Ceramics Laboratory
Directorate of Materials and Processes

iii

CONTENTS

LIST OF FIGURES

v

I. INTRODUCTION

The application of heat-treatable steels in structures at ultra-high strength levels in recent years has pointed to their susceptibility to brittle fracture as a major problem. This research was initiated as a result of curiosity about the relatively large number of steel compositions developed for application at tensile strength levels above 225,000 psi. The question asked was whether or not the various steel compositions heat treated to a given strength level vary significantly in their susceptibility to initiation and propagation to fracture and if such differences can be correlated to certain features of the microstructures.

The susceptibility to ductile fracture is proposed to be related to susceptibility to plastic instability, or highly localized flow. This susceptibility for six selected steel compositions was tested in torsion at tensile strength levels of 250,000 and 275,000 psi. Companion true stress-true strain tensile tests were made for cross correlation. Preliminary propagation tests were made on bend specimens in which the total available energy is controllable. The microstructures of the experimental steels were studied by optical microscopy, electron microscopy, and electron diffraction.

II. EXPERIMENTAL STEELS

A. AISI 4340 STEEL

This material was obtained in the form of 1¼ inch diameter rods from Republic Steel Corporation, Massilon, Ohio. The chemical composition is given in Table I.

B. 300 M STEEL

This material was obtained in the form of 1¼ inch diameter rods from Republic Steel Corporation, Massilon, Ohio. The chemical composition is shown in Table I. The steel is a modification of AISI 4340 containing an increased silicon and vanadium content which allows tempering at a comparatively high temperature by raising the embrittlement temperature range.

C. LADISH D6A, D6AC

These materials were obtained in the form of 1¼ inch diameter rods from Republic Steel Corporation, Massilon, Ohio. The chemical compositions are given in Table I. D6A is an air-melted steel. D6AC is a vacuum consumable electrode arc melted steel. They are both air hardenable.

D. H-11 STEELS

These materials were obtained in the form of ¾ inch diameter rods from Vanadium Alloys Steel Company both in air melted and vacuum consumable

Table I. Chemical Composition of the Experimental Steels

Grade	Supplier	Melting Procedure	Heet Number	Chemical Composition % Wt.														
				O₂	H₂	N₂	C	Mn	P	S	Si	Cu	Ni	Cr	Mo	V	Co	Al
AISI 4340	Republic	In air	3351175				0.40	0.75	0.008	0.01	0.29		1.76	0.73	0.24			
300M	Republic	In air	B59945				0.42	0.85	0.007	0.012	1.56		1.80	0.81	0.48	0.10		
D6A	Republic	In air	3330492				0.45	0.84	0.009	0.011	0.30			1.03	1.01	0.10		
D6AC	Republic	In vacuum	3950446				0.45	0.76	0.007	0.007	0.23			1.02	1.04	0.08		
H-11	Vanadium Alloy Steel Corp.	In air	31951				0.39	0.33	0.017	0.008	0.94			5.08	1.30	0.53		
H-11	Vanadium Alloy Steel Corp.	In vacuum	05568				0.40	0.24	0.010	0.010	0.95			5.16	1.40	0.48		
Mx-2	Mellon Institute	Single vacuum		9 ppm*	1.1 ppm	0.013	0.40	0.64	0.010	0.006	0.93	0.040	0.045	0.99		0.15	1.07	0.045
Mx-2	Mellon Institute	Double vacuum		12 ppm	1.8 ppm	0.011	0.41	0.59	0.008	0.006	0.89	0.042	0.045	1.01	0.29	0.14	1.07	0.035
Hy-Tuf	Crucible Steel Co.	In air	114070				0.25	1.37	0.014	0.011	1.37		1.79	0.39	0.39			

*ppm = parts per million obtained by vacuum fusion.

electrode arc melted condition. They are also known as Vascojet 1000, which is a modification of the popular hot work die steel called Hot Form (AISI designation is H-11). The outstanding features are deep hardenability by air cooling and a secondary hardness peak that appears in the vicinity of 950°F. Tempering is conducted at still higher temperatures. Multiple tempering in this range transforms essentially all of the retained austenite to tempered martensite. The chemical compositions are given in Table I.

E. MX-2 STEELS

These materials were obtained through the courtesy of Dr. G. K. Bhat and Mr. E. Vandale of the Mellon Institute in the form of $1\frac{1}{4}$ inch and $\frac{5}{8}$ inch diameter rods, both in single vacuum consumable arc melted and double vacuum consumable arc melted form. The steels are modified essentially by addition of one per cent each of cobalt and silicon. Multiple tempering is recommended. There is a temper embrittlement range found with this alloy, whose peak exists at 700°F. The chemical compositions of the steels are given in Table I.

F. HY-TUF STEEL

This material was obtained in the form of $\frac{3}{4}$ inch diameter rods from Crucible Steel Company. The nominal composition is given in Table I. This alloy was designed for   use under 240,000 psi ultimate tensile strength level.

III. MECHANICAL TESTING

A. TENSION TESTS

All tests were conducted at ambient temperature and the specimens were heat treated to ultimate tensile strengths of 250,000 psi and 275,000 psi. The object of tension testing was principally to ascertain the tempering temperatures for obtaining the established strength levels and to correlate the strain-hardening characteristics and the plastic instability in simple tension to these properties deduced from the torsion tests. The code identification of experimental steels is given in Table II.

1. Preparation of Tensile Specimens

The proportionate size (1) of threaded-end round tension test specimens with 1 inch gage length and $\frac{1}{4}$ inch diameter were used throughout the tension testing. Three specimens of each steel at each strength level were prepared as follows:

< 1 > Normalize   2 hrs. total

< 2 > Temper $1\frac{1}{2}$ hrs. total

3

Table II. Code Identification of the Experimental Steels

Steel Designation	Commercial Name	Melting Procedure
A	AISI 4340	In air
B	300M	In air
C	D6A	In air
CV	D6AC	Vacuum consumable arc
D	H-11	In air
DV	H-11	Vacuum melted
E	MX-2	Single vacuum consumable electrode
EV	MX-2	Double vacuum consumable electrode
F	Hy-Tuf	In air

< 3 > Rough machine to 0.275 inch diameter (0.325 inch diameter for torsion specimens).

< 4 > Austenitize   1 hr. total

< 5 > Quench

< 6 > Temper to established strength levels

< 7 > Finish machine to standard 0.25 inch, 0.50 inch diameter tensiles (0.300 inch diameter for torsion specimens).

< 8 > Stress relieve   1 hr.

Results of the preliminary tensile tests for obtaining the proper tempering temperatures in the experimental steels are given in Table III. Grain size has been checked on steels AISI 4340 and H-11 after austenitizing for one hour. Both steels yielded the same value, namely, ASTM No. 8. Based upon the data shown in Table III, the relations of tempering temperatures and ultimate tensile strengths have been drawn as shown in Figure 1. Proper tempering temperatures for tensile strength levels of 250,000 psi and 275,000 psi were obtained by extrapolation. The determined heat treatments for obtaining the established strength levels in experimental steels are shown in Table IV according to which both tension and torsion specimens were made.

2. Method of Testing

Tension tests were conducted in a Tinius Olsen Universal Testing Machine using the 30,000 lb. load capacity. The speed of the cross head was maintained constant at 0.0112 inch per minute which is equivalent to a strain rate of 0.0112 inch per minute for a gage length of one inch. As soon as the loaded specimen reached the yielding point, load-diameter measurements were recorded to fracture. A micrometer gage was used to measure the change of diameter. Care was exercised in the initial stage of loading to locate the smallest cross-sectional area by moving the gage over the entire gage length of the specimen. Formulae for calculating true stress and true strain from the measured data have been illustrated in many publications. (2,3,4)

3. Results and Discussion

According to the maximum load conception of instability, a relation between plastic instability and strain-hardening characteristics in pure tension can be derived from the empirical relation between true stress and true strain.

$$\sigma = K\delta^n \tag{1}$$

5

Table III. Results of Preliminary Tensile Tests for Obtaining Proper Tempering Temperature in the Experimental Steels

Specimen Number*	Austenitizing Temp., °F	Austenitizing Time, hr.	Quenching Medium	Tempering Temp., °F	Tempering Time, hr.	Tempering Cycle	Stress Relieving Temp., °F	Stress Relieving Time, hr.	Tensile Strength Psi	Yield Strength (0.2% offset) Psi	Reduction Area %	Elongation (1" g.l.) %
TA2	1525±5	1	No. 2 oil	450±10	1	Single	350	1	277,500	236,300	37.2	11.1
TA3	1525±5	1	No. 2 oil	550±10	1	Single	350	1	250,500	214,900	44.8	11.9
TA4	1525±5	1	No. 2 oil	650±10	1	Single	350	1	233,100	213,300	46.2	12.6
TB1	1600±5	1	No. 2 oil	650±10	1	Double	500	1	292,600	255,700	41.7	13.4
TB3	1600±5	1	No. 2 oil	860±10	1	Double	500	1	252,100	217,400	45.3	12.2
TB4	1600±5	1	No. 2 oil	800±10	1	Double	500	1	263,800	220,400	43.5	12
TC1	1550±5	1	Air	600±10	2	Double	500	1	263,700	229,500	36.8	11.5
TCV1	1550±5	1	Air	600±10	2	Double	500	1	267,500	234,400	47.9	14
TC2	1550±5	1	Air	650±10	2	Double	500	1	255,000	226,400	41.5	11.4
TCV2	1550±5	1	Air	650±10	2	Double	500	1	255,800	234,400	46.7	10.8
TC3	1550±5	1	Air	750±10	2	Double	500	1	246,400	223,300	41.6	12.4
TCV3	1550±5	1	Air	750±10	2	Double	500	1	248,200	231,700	47.4	14.9
TD6	1850±5	1	Air	1020±5	2	Double	900	1	264,200	223,500	30.1	12.5
TDV6	1850±5	1	Air	1020±5	2	Double	900	1	274,000	238,300	9.9	5
TD7	1850±5	1	Air	990±5	2	Double	900	1	285,000	244,300	30.7	8.5
TDV7	1850±5	1	Air	990±5	2	Double	900	1	293,000	254,100	27.6	10
TD16	1850±5	1	Air	1080±10	2	Double	900	1	229,000	192,400	35.6	10.5
TDV16	1850±5	1	Air	1080±10	2	Double	900	1	236,400	197,800	25	8.5
TE2	1700±5	1	No. 2 oil	530±10	2	Double	400	1	279,400	243,200	36	10
TEV2	1700±5	1	No. 2 oil	530±10	2	Double	400	1	279,100	244,000	34.8	12
TE3	1700±5	1	No. 2 oil	590±10	2	Double	400	1	269,700	228,100	35.8	12
TEV3	1700±5	1	No. 2 oil	590±10	2	Double	400	1	267,900	229,200	57.4	11
TE4	1700±5	1	No. 2 oil	680±15	2	Double	400	1	246,100	223,600	36.9	11.8
TEV4	1700±5	1	No. 2 oil	680±15	2	Double	400	1	246,800	223,100	36.3	10
TF1	1600±5	1	No. 2 oil	450±10	2	Single	200	1	240,600	220,800	45.8	13.1
TF3	1600±5	1	No. 2 oil	300±15	2	Single	200	1	273,200	245,300	41.8	12.1
TF4	1600±5	1	No. 2 oil	400±15	2	Single	200	1	254,400	230,900	45.5	12.7

*These designations correspond to those in Table II except that a T is prefixed for tension test.

6
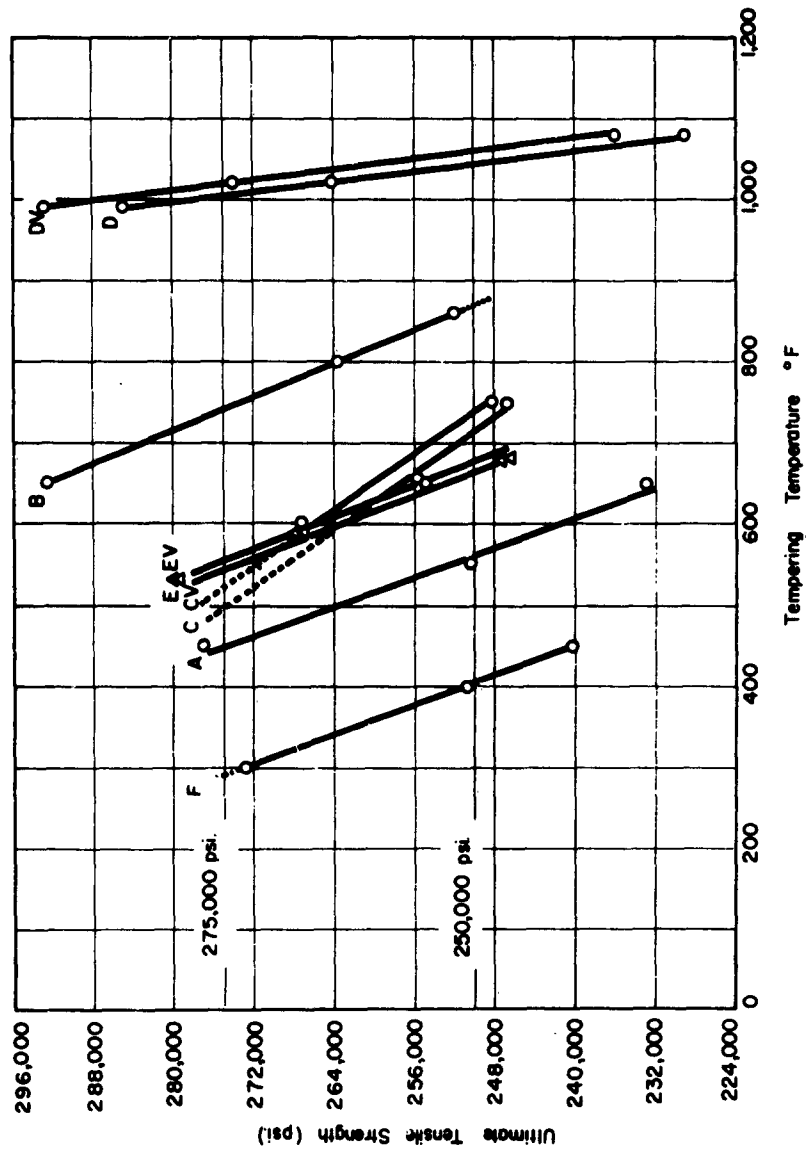
Figure 1. Tempering Curves for the Experimental Steels

7

Table IV. Proper Heat Treatment for Obtaining Established Strength Levels in the Experimental Steels

Series*	Hardening		Quenching Medium	Tempering		Stress Relieving		Hardness after Tempering Rc
	Temp., °F	Time, hr.		Temp., °F	Time, hr.	Temp., °F	Time, hr.	
TA6	1525±10	1	oil	450±15	1	350	1	52-53
TA15	1525±10	1	oil	550±15	1	350	1	49-50
TB5	1600±5	1	oil	740±10	1+1	500	1	51-52
TB15	1600±5	1	oil	870±10	1+1	500	1	48-49
TC5	1550±5	1	air	510±10	2+2	400	1	52-53
TC15	1550±5	1	air	720±10	2+2	400	1	48-49
TCV5	1550±5	1	air	510±10	2+2	400	1	52-53
TCV15	1550±5	1	air	720±10	2+2	400	1	48-49
TD8	1850±5	1	air	1010±5	2+2	900	1	53
TD18	1850±5	1	air	1060±5	2+2	900	1	49-50
TDV8	1850±5	1	air	1010±5	2+2	900	1	53
TDV18	1850±5	1	air	1060±5	2+2	900	1	49-50
TE6	1700±5	1	oil	530±10	2+2	400	1	53
TE16	1700±5	1	oil	680±10	2+2	400	1	48-49
TEV6	1700±5	1	oil	530±10	2+2	400	1	52
TEV16	1700±5	1	oil	680±10	2+2	400	1	49
TF5	1600±5	1	oil	300±15	2	200	2	51
TF15	1600±5	1	oil	400±15	2	200	2	48-49
TCV8R**	1500±5	1	air	510±10	2+2	400	1	51-52
TCV9R	1500±5	1	air	510±10	2+2	400	1	51-52

*These designations correspond to those in Table II except that a T is prefixed for tension test.

    AX, BX ... FX = Specimen series of high strength level
                    275,000 psi.
    AXY, BXY ... FXY = Specimen series of low strength level
                    250,000 psi.

**Specimens used for obtaining reproducibility.

from which it follows that

$$\delta_{m\ell} = n \tag{2}$$

where n is the strain hardening exponent, K is strength coefficient, σ and δ are true stress and true strain, and $\delta_{m\ell}$ is the true strain at the maximum load. Thus, the true strain at which necking begins to form in uniaxial tension is equal to the strain-hardening exponent, provided equation (1) is valid. Experimentally, it was found that when the load reaches a maximum, the strained specimen tends to maintain the maximum load for a short period of time. Hence, it was possible to record several readings in the change of diameter at this transient stage of maximum load. One of the strain values obtained during this period corresponds to the strain-hardening exponent. The test results which correlate strain at maximum load to its strain-hardening exponent are shown in Table V along with other important tensile properties. It appeared that necking starts at the end of maximum load period. The reproducibility of the tensile properties was determined by two repetitive tests of steel D6AC at a high strength level. These two tests are labeled as TCV8R and TCV9R listed at the bottom of Table V. A good reproducibility of tensile properties was obtained as can be seen for specimens TCV5, TCV8R and TCV9R. The true fracture stress, which is defined as the load at fracture divided by the cross-sectional area at fracture, is listed here only for reference. Actually this stress should be corrected for the triaxial state of stress existing in the tensile specimen at fracture. Since the primary purpose of the test is to determine the relations involved in strain-hardening characteristics and plastic instability, the fracture stresses were not corrected for triaxiality.

The strain-hardening characteristics n, and K were obtained by plotting first the true stress-true strain data on a log-log paper. Typical plots are presented in Figure 2. At the beginning of the plots, deviations from the empirical equation (1) were frequently observed. One common type of deviation is a curve with continuously decreasing slope which can be readily seen in Figure 3 by plotting the slope of the log true stress-true strain curve as a function of true strain. The slopes of the log true stress-true strain curves or the strain-hardening exponents were obtained graphically as described by Low (5). The departure from a straight line at both small and large strains was also noted by Marin who has proposed a correction method (6). Since these deviations practically do not affect the processing of tensile data for obtaining strain-hardening exponents, the representative values of n and K were obtained by treating that portion of the log true stress-true strain curve in which equation $\sigma = K\delta^n$ is valid. These regions are marked with two arrows in each plot. Calculations of n and K were carried out by using the least-squares method. Results so obtained agree consistently with those values obtained graphically. Values of n and K are also presented in Table V. There is reasonably good agreement between n and $\delta_{m\ell}$. The flatness of the stress-strain curve in the vicinity of the maximum load point caused some uncertainty in determining $\delta_{m\ell}$. It was generally computed from the cross-sectional area when the load started decreasing.

9

Table V. Tensile Properties of the Experimental Steels

Steel Desig- nation*	Expected Strength Level (1000 psi)	Actual Tensile Strength (psi)	Yield Strength (0.2%) (psi)	Elongation (1 inch) (%)	Reduc- tion Area (%)	True Stress-True Strain Properties						
						$\sigma_{.04}$ (psi)	σ_{ml} (psi)	δ_{ml}	σ_f (psi)	δ_f	n	K (psi)
TA6	275±5	270,400	236,800	11.6	39.2	267,600	289,600	0.050	386,300	0.486	0.064	348,500
TA16	250±5	249,200	215,200	12.0	41.2	247,700	250,200	0.070	305,200	0.597	0.071	327,000
TB5	275±5	272,300	242,500	10.1	57.1	279,800	288,100	0.054-0.070	360,900	0.483	0.078	362,000
TB15	250±5	245,200	218,100	15.2	39.6	249,200	255,100	0.056-0.073	336,100	0.554	0.081	318,000
TC5	275±5	278,900	247,900	7.5	34.2	289,600	294,500	0.036	358,600	0.455	0.040	336,000
TC15	250±5	245,200	218,000	12.2	41.6	252,900	252,900	0.056	322,800	0.566	0.052	300,000
TCV5	275±5	279,200	246,900	11.0	44.1	289,100	292,500	0.044-0.052	388,500	0.666	0.044	341,000
TCV15	250±5	246,100	219,300	13.2	46.9	254,700	256,500	0.046-0.058	317,200	0.624	0.047	296,000
TD8	275±5	279,400	245,200	7.5	21.7	293,200	293,200	0.040	332,100	0.358	0.044	342,000
TD18	250±5	245,400	219,500	10.5	32.6	253,500	259,500	0.048-0.073	318,200	0.471	0.061	311,000
TDV8	275±5	278,600	241,200	8.1	24.2	290,900	290,900	0.042-0.051	338,000	0.365	0.045	357,000
TDY18	250±5	245,900	219,400	11.1	31.3	255,600	260,000	0.040-0.073	311,300	0.416	0.056	310,000
TB6	275±5	279,400	243,200	10.0	36.5	290,800	290,800	0.040-0.048	360,000	0.447	0.044	335,000
TB16	250±5	246,100	214,600	11.8	36.9	255,100	259,800	0.046-0.054	316,500	0.463	0.058	307,000
TBV6	275±5	279,100	244,500	10.7	34.8	291,100	291,100	0.041-0.050	364,900	0.431	0.046	332,000
TBV16	250±5	246,800	214,200	11.0	36.3	255,600	260,400	0.045-0.053	318,400	0.452	0.056	304,000
TF5	275±5	270,800	239,800	13.0	43.8	279,300	290,500	0.061-0.070	388,100	0.607	0.070	353,000
TF15	250±5	246,300	214,300	13.8	52.0	254,500	264,700	0.054-0.071	285,800	0.759	0.072	320,000
TCV8R	275±5	276,800	244,000	11.0	46.5	285,700	283,700	0.042-0.051	375,300	0.666	0.043	324,000
TCV9R	275±5	274,900	240,800	11.3	47.3	282,800	282,800	0.042-0.046	376,800	0.673	0.044	326,000

*These designations correspond to those in Table IV.

Definition of symbols:

$\sigma_{.04}$ = true stress at true strain of 0.04

σ_{ml} = true stress at maximum load

δ_{ml} = true strain at maximum load

σ_f = true fracture stress

δ_f = true fracture strain

n = strain hardening exponent

K = strength coefficient
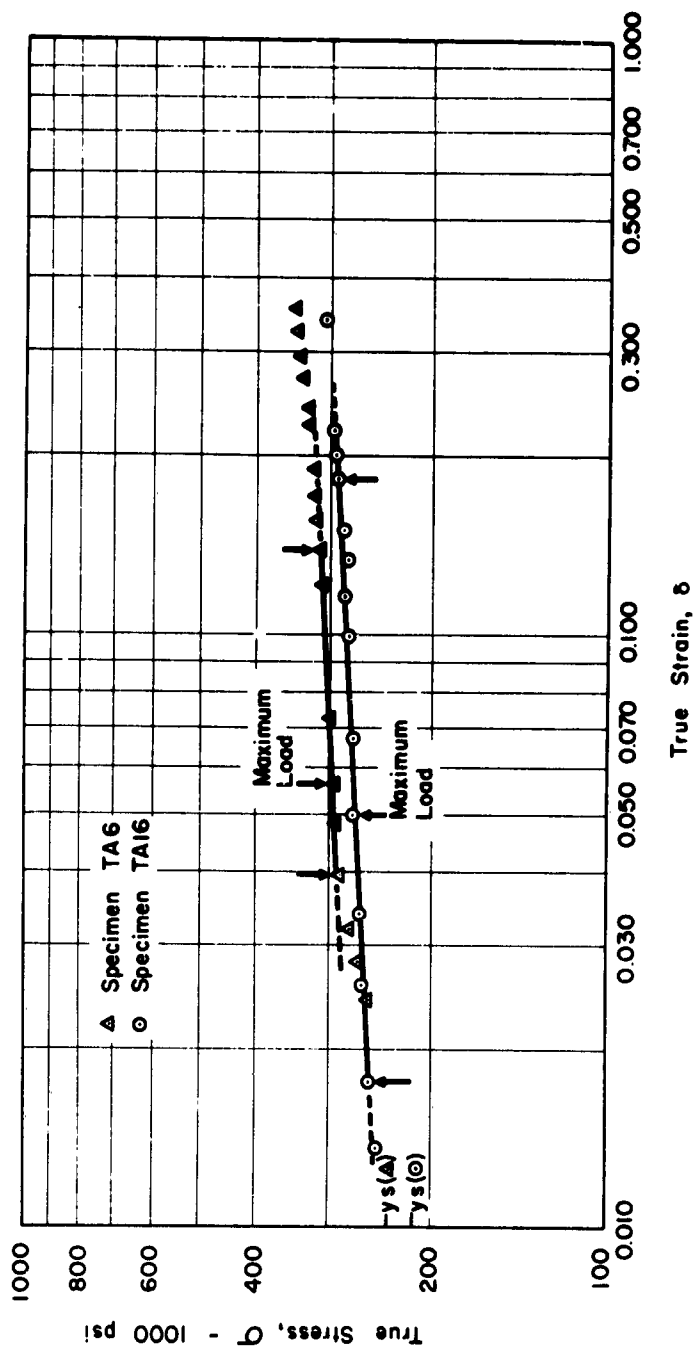
Figure 2. Log Stress-Log Strain Plots for Steel AISI 4340 Heat Treated to Strength Levels of 250,000 psi and 275,000 psi. The two extreme arrows on each curve indicate the region where equation $\sigma = K\delta^n$ is valid.

11
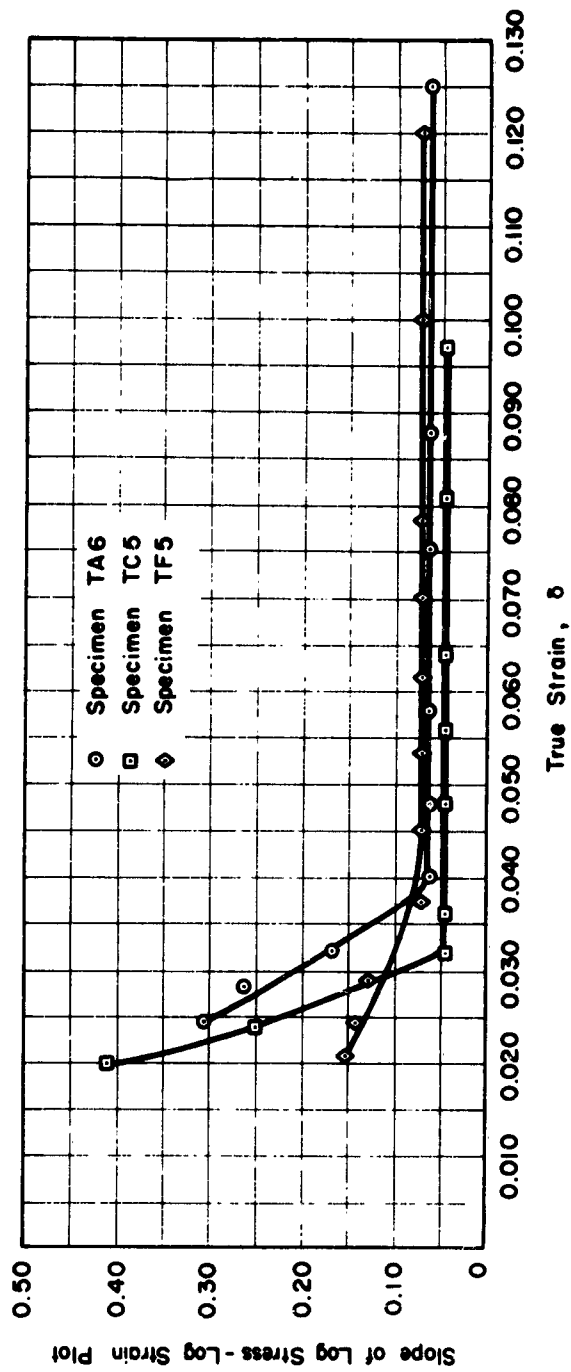
Figure 3. Selected Experimental Results on the Variation of the
Apparent Strain Hardening Exponent with True Strain

B. TORSION TESTS

1. Torsion Test Apparatus

The torsion test was conducted in a specially designed torsion tester as shown in Figure 4. The applied torque was measured through a load cell of tubular cross section on which four A-7 type wire resistance strain gages were mounted. The gages were positioned at an angle of 45° to the axis of the tubular section and were connected electrically in the form of a wheatstone bridge circuit with two gages in tension and two in compression as the torque was applied to the load cell. The change in resistance occurring in the strain gage was measured by a "DIGITAL STRAIN INDICATOR" which was shown in the right-hand side of the torsion apparatus in Figure 4. The load cell was calibrated against a set of known dead weights and a predetermined lever arm. The output (strain on the indicator) was found to be linear with applied torque as presented in Figure 5 and the calibration curve was reproducible to within 0.5 per cent.

Torque transmission was supplied by a 1750 rpm, $\frac{1}{2}$ hp electric motor which drove a 200:1 reductor which in turn drove a 600:1 reductor. The movable base of the electric motor with this particular combination of motor and reductors permitted a range of strain rates from 0.0$\overset{\cdot}{\mathstrut}$4 inch to 0.103 $(min)^{-1}$.

2. Preparation of Torsion Specimens

Three to five specimens of each steel of each strength level established in the tension test were studied in order to obtain good reproducible values of the measurements to be correlated. A sketch of the specimen is given in Figure 6. The processing and heat-treatment procedures used in preparing torsion specimens were essentially the same as those used in making tension specimens as given in Table IV, except that each torsion specimen after stress relief was finished by polishing with 5-micron diamond dust throughout the gage length. The uniformity of diameter within the gage length was important because it was necessary to detect the onset of localized deformation and its further development employing a surface replica technique (7).

3. Method of Testing

An optical microscope set at 100X was erected above the specimen and used as a device to detect the onset of localized deformation or the change from uniform plastic deformation to localized plastic deformation. The test was conducted continuously to fracture. The preliminary torque twist data were obtained in such a manner that within the elastic range, readings on the strain indicator were recorded at each increment of angle of twist of one degree. After reaching the yield point, torque readings were recorded at every two degrees of angle of twist. At the same time the surface of the specimen was examined along the gage length with the optical
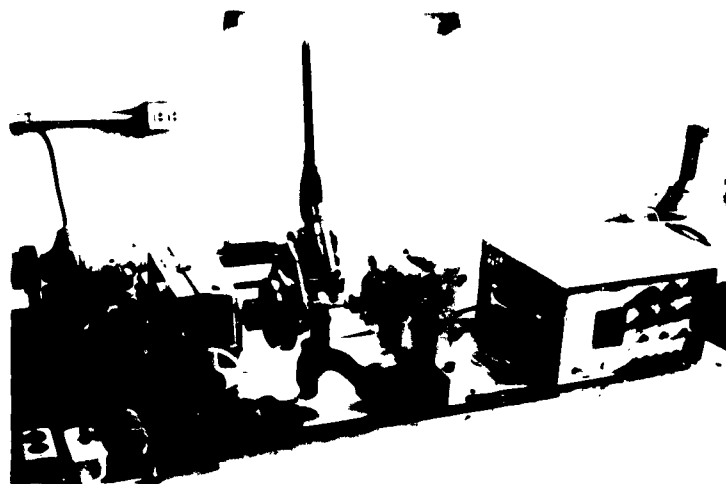
Figure 4.   General View of Torsion Test Apparatus

14
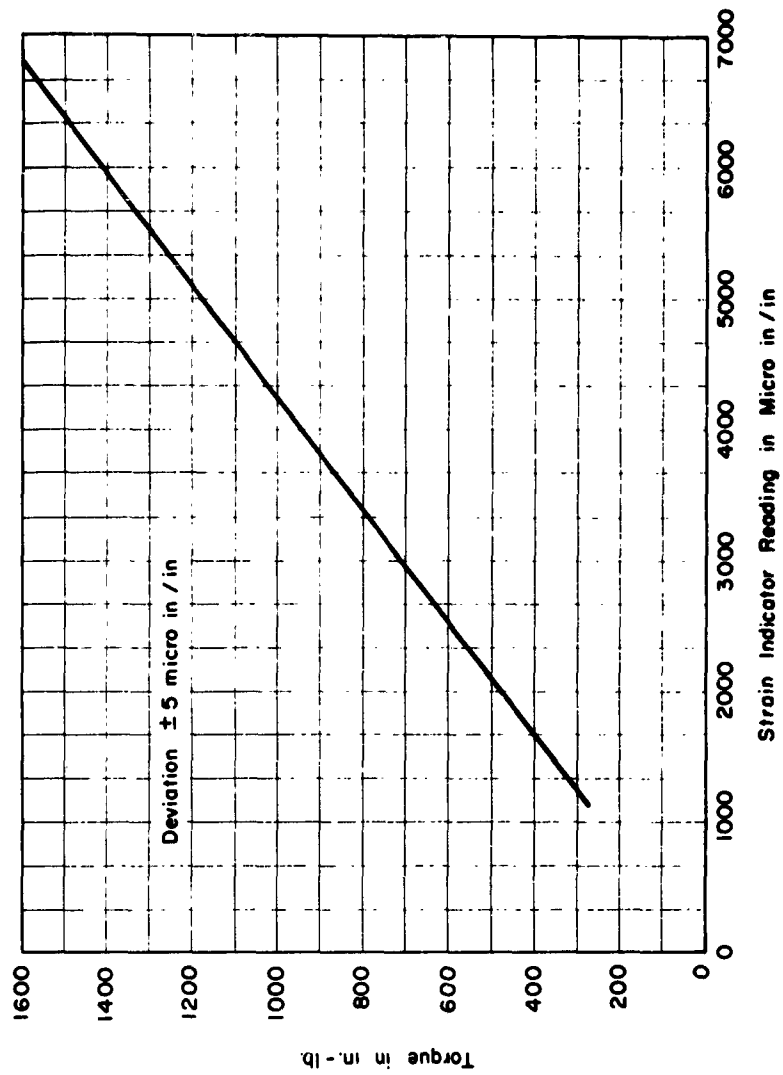
Figure 5. Calibration Curve for Torsion Tester

15
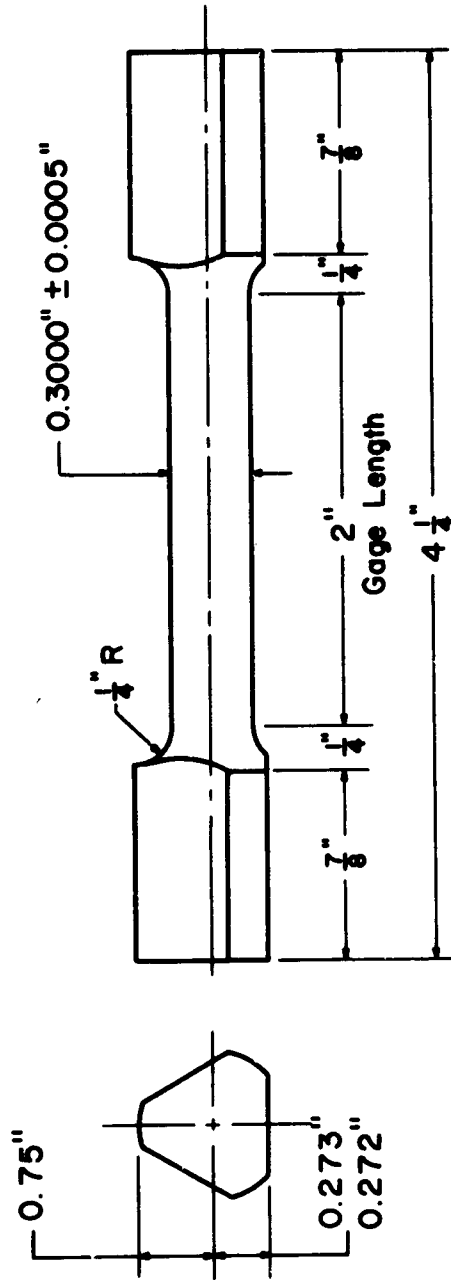
Figure 6. Sketch of the Torsion Specimen

16

microscope. It was found that small flow figures resembling Lüders' lines
(8, 9) appeared on the polished surface and then distributed themselves
evenly along the gage length. As straining continued, the flow figures
usually propagated in a transverse direction and the appearance of the flow
figures became intensified. The first manifestation of a localized defor-
mation zone was detected by the coalesence of these flow figures to such
an extent that the localized zone could be recognized easily by the optical
microscope. Also it appeared that the specimen had a localized deformation
zone as described by Polakowski (10). The strain in this stage was recorded
and referred to as the amount of uniform strain or instability strain in
torsion. After the onset of localized deformation the zone generally ex-
panded longitudinally by coalesence of more of these flow figures. In some
specimens, the localized deformation zone which was first initiated during
the onset stage would stop expanding. A second localized deformation zone
was then initiated preceded by a slight drop of load (2 in-lbs to 6 in-lbs),
after which the expansion of the localized deformation zone resumed its
usual manner with a slight increase of load as twist continued. The forma-
tion of localized deformation zones is well illustrated in Figure 7 in which
specimen F3 represents its onset stage. Specimen O shows the specimen before
testing. The length of expansion of the localized deformation zone which
varied with the grade of steel is illustrated by the rest of the specimens
in the same figure.

4. Results and Discussions

In the construction of shear stress-strain curves for each steel
tested, the analytical treatment of torque-twist data described by Nadai (11)
was used. The torque-twist curve $M = f(\theta)$ was drawn from the initial torque-
twist data taken during the test. The final shear stress-strain curve $\tau = f(\gamma)$
may be determined from the equation

$$M\theta^3 = 2\pi \int_0^{\gamma_a} f(\gamma)\gamma^2 d\gamma \qquad (3)$$

where M represents applied torque; θ is the angle of twist of the specimen
per unit length; γ denotes shear strain, and γ_a is the shear strain where
the radius of the specimen equals a. The right side of the equation (3) is
a function of the upper limit γ_a and since $\gamma_a = a\theta$, it is also a function of
θ. After differentiating (3) with respect to θ the following equation yields

$$\tau_a = \frac{1}{2\pi a^3} \left[\theta \frac{dM}{d\theta} + 3M \right] \qquad (4)$$

This equation serves for determining the shear stress-strain curve $\tau = f(\gamma)$
of a round bar if the torque-twist curve $M = f(\theta)$ was obtained in the torsion

17
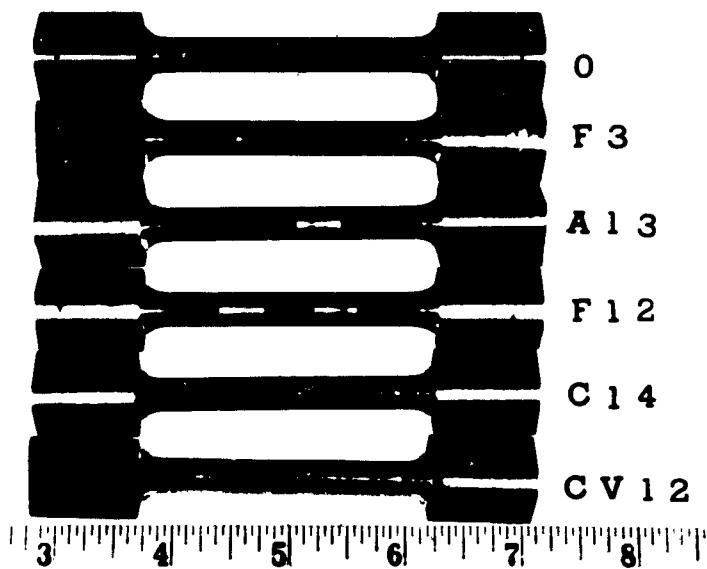
Figure 7. The Onset and Expansion Stage
of Localized Deformation Zone

18

test. The computation of shear stress is finally obtained by drawing the tangents to the torque-twist curve and measuring the intercept of the tangent to the torque ordinate (12). Since the graphical solution described above was a very slow and laborious process and also involved the introduction of additional errors by determining the slope $dM/d\theta$, a numerical method which would both accelerate the processing of the data and assure the highest accuracy of the derived quantities was developed. The numerical method which was used in constructing the shear stress-strain curves was initially suggested by Professor Paul A. Graham of the Department of Engineering Mechanics of the Ohio State University. The preliminary torque-twist data are processed in a computer from which the final shear stress-strain data are obtained. The construction of shear stress-shear strain curves was completed by means of an automatic plotter. Typical shear stress-shear strain diagrams are presented in Figure 8. In each figure, two additional shear stress-shear strain curves corresponding to the two strength levels were drawn from the tensile flow curves converted to the stress state of torsion. The conversion of tensile data to shear stress-shear strain values was made by using the significant stress and significant strain relationships, from which the following equations result:

$$\tau_c = \frac{\sigma_1}{\sqrt{3}} \tag{5}$$

$$\gamma_c = \sqrt{3}\, \epsilon_1 \tag{6}$$

where τ_c and γ_c are the converted shear stress and shear strain; σ_1 and ϵ_1 are the true stress and true strain in simple tension. The true-stress values beyond the maximum load point were corrected for the triaxial state of stress by using Siebel's formula (13). The corrected true stress was then substituted in equation (5).

Since the use of a numerical method in treating torsion data was essentially based on the derivative quantities of the experimental data, any minor fluctuation of the load experienced in the preliminary torque-twist data would be magnified in the final shear stress-shear strain curves as shown in Figure 8. The peak regions in the shear stress-strain curve B4 usually correspond to a jump of the preliminary torque-twist plot as shown under those shear stress-strain curves in the same figure. This jump of load in most specimens corresponds to initiation of a new localized deformation zone accompanied by a minor fluctuation of the load. It is likely that the weak regions of the specimen induced either by the chemical inhomogeneity in the steel or the structural discontinuity introduced by the heat treatment are the main causes of the fluctuation of the load. Various patterns of the expansion of the localized deformation zones as shown in Figure (have shown that expansion at both ends of the localized deformation zone was favorable. Examination with the microscope revealed that the coalescence of flow figures is related to the expansion of the localized deformation zone.

19

Shear Stress τ-1000 psi, Torque M-10 in-lbs

γ_ins (Tension)

γ_ins (Torsion)

γ_ins (Torsion)

γ_ins (Tension)

● B4 (Torsion)
○ B11 (")
△ TB5 (Tension)
□ TB15 (")
○ B4 (Torque-Twist Curve)

Shear Strain γ

Figure 8.   Shear Stress-Strain Curves in Torsion and Converted Shear Stress-Strain Curves from Tension for Steel 300 M at Strength Levels of 250,000 psi and 275,000 psi. (The preliminary torque-twist plot from which shear stress-strain curve was obtained is shown under the shear stress-strain curves. γ_ins is the amount of shear strain at the onset of unstable plastic strain.
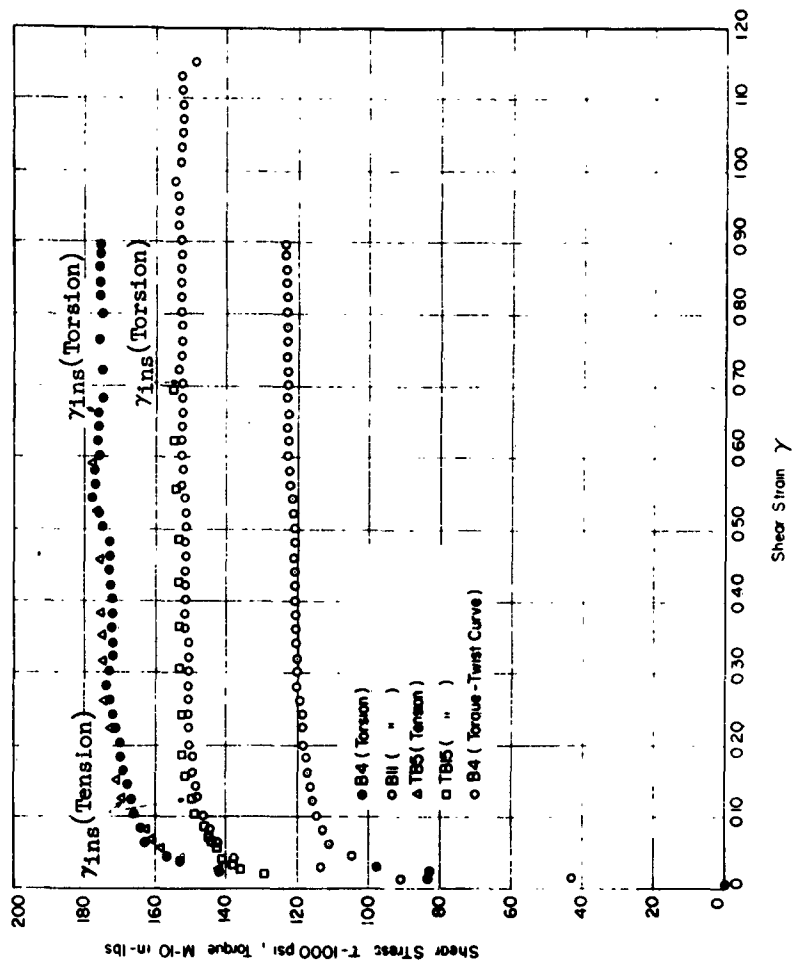
20

The onset of fracture can occur in any expansion pattern of the localized deformation zone as given in Figure 7. Evidently the total amount of plastic strain in torsion can be varied enormously from steel to steel. Throughout the test, fracture always initiates at the front of the advancing localized deformation zone as shown in Figure 9 (see arrow).

Two representative torsion test parameters were selected on a basis of reproducibility. These are the amount of uniform strain prior to the onset of localized deformation zone and the total plastic strain to fracture. The experimental results of the two representative parameters are shown in Table VI. By consideration of the table, it is apparent that some of the results are hardly reproducible in their total amount of plastic strain to fracture. This inconsistency became worse in the specimens of lower strength levels. Outstanding examples are specimens A14, A15, C12, C15, CV12, and CV13. Thus, the length of the expanded localized deformation zone can be varied to a great extent in the same steel heat treated to the same strength level. This inconsistency suggests that material discontinuity induced either by variation of chemistry or the processing of the steel can be related to the length of localized deformation zone or the total plastic strain. The results given in Table VI revealed also the fact that specimens of lower strength level tend to develop a larger range of localized deformation zone as compared with those in the high strength level.

Although the exact conditions under which fluctuations of the load were produced are not quite clear, there is little doubt they are a manifestation of strain hardening characteristics of the steels tested.

The shift of the localized deformation zone as shown in Figure 7, specimen F3, was always preceded by a decreasing of the load, normally about 2 inch-lb to 6 inch-lb depending upon the grade of steel. As soon as the newly emerged localized deformation zone became visible, the load first resumed its original value and then increased to a higher load (about 3 in-lb more). This sort of fluctuation of the load was first found in mild steel in tension tests. Elam (14) observed similar fluctuations of the load in a quenched aluminum alloy. She found that fluctuation of the load started after a certain strain was reached. At the same time the bar became uneven, proving that the yielding under these circumstances progressed in steps through the formation of discrete slip bands during each fluctuation of the load. In torsion, similar phenomena have also been observed by Polakowski (10) in cold-drawn copper, iron, and some of their alloys as well as quenched and tempered AISI 4340 steel.

In order to classify the results conveniently, the experimental steels which have exhibited such a fluctuation of the load accompanied by a visible localized deformation zone as shown in Figure 10 are referred to as class A. Since the plastic instability in torsion is defined as the change of uniform plastic deformation to localized plastic deformation, class A has the characteristics of discernible instability. Steels AISI 4340, D6AC, Hy-Tuf heat treated to both strength levels and Mx-2 heat treated to lower strength level belong to this category. No recognizable localized deformation zone has been observed in steel H-11 at both strength levels. After

21
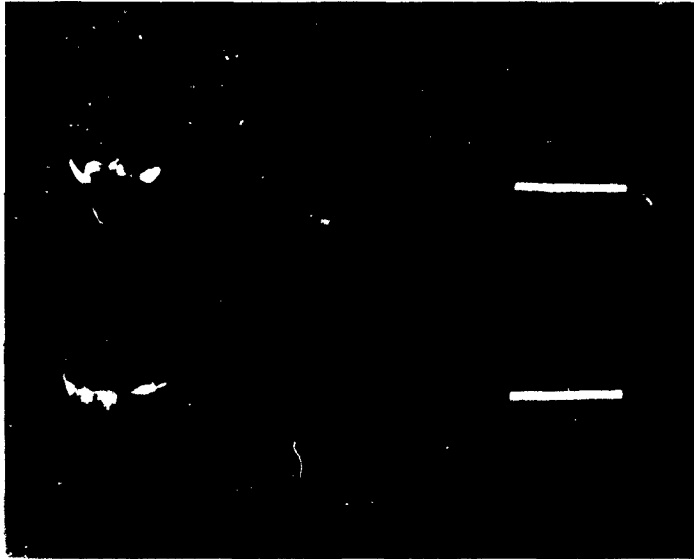
Figure 9.   Typical Shear Mode Fracture
of the Torsion Specimen

Table VI. Torsion Properties of Experimental Steels

Test Specimen	Tensile Strength Level (psi)	$\tau_{0.01}$ (psi)	γ_u (in/in)	γ_t (in/in)
A8	270,400	151,800	0.097	0.348
A9	270,400	151,400	0.099	0.332
A14	249,200	140,000	0.111	0.609
A15	249,200	141,000	0.128	0.998
B4	272,300	151,500	0.651	0.893
B5	272,300	153,500	0.674	0.873
B11	245,200	134,200	0.703	1.144
B15	245,200	135,000	0.705	1.055
C2	278,900	160,500	0.115	0.151
C3	278,900	165,000	0.112	0.167
C12	245,200	153,500	0.148	0.462
C15	245,200	152,700	0.125	0.175
CV1	279,200	164,200	0.104	0.190
CV3	279,200	164,000	0.133	0.203
CV12	246,100	150,700	0.138	0.910
CV13	246,100	154,700	0.138	0.428
D4	279,400	151,200	0.705	0.705
D5	279,400	151,000	0.909	0.909
D15	245,400	134,800	0.776	0.776
D16	245,400	137,500	0.707	0.707
DV4	278,600	160,600	0.556	0.556
DV5	278,600	156,800	0.543	0.543
DV14	245,900	139,600	0.689	0.689
DV16	245,900	141,000	0.530	0.530
E4	279,400	157,000	0.276	0.420
E6	279,400	159,500	0.284	0.446
E15	246,100	141,600	0.352	0.637
E16	246,100	144,300	0.352	0.522
EV4	279,100	160,000	0.268	0.354
EV6	279,100	158,000	0.258	0.443
EV15	246,800	143,600	0.273	0.375
EV16	246,800	145,000	0.266	0.455
F2	270,800	138,000	0.413	0.445
F3	270,800	139,600	0.411	0.452
F12	246,300	133,000	0.404	0.634
F13	246,300	136,000	0.407	0.619

Definition of symbols: $\tau_{0.01}$ = shear stress at shear strain 0.01.

                                   γ_u = uniform shear strain at which localized deformation occurs.

                                   γ_t = total shear strain.

A 1 3

C 1 4

C V 1 2

E 1 5

E V 1 4

F 1 2

Figure 10. Class A - Discernible Instability Exihibited in
Steels AISI 4340, D6A, D6AC, Hy-Tuf at Both
Strength Levels and Mx-2 at Lower Strength Level

yielding, the deformed region of this grade of steel assumed a cloudy appearance in which flow figures were developed evenly along the gage length as can be seen in Figure 11 with the unstrained specimen O shown at the top. A particularly interesting observation in testing of this grade of steel was that no appreciable fluctuation of the load was observed. By comparing the strain-hardening exponents as given in Table V, steel H-11 has a smaller value than those steels pertinent to class A. For the time being, this particular mode of plastic behavior typified by a vague manner of instability phenomenon is referred to as class B.

In steels 300M at both strength levels and Mx-2 at high strength level, the behavior of class A was observed. However, as soon as the specimen started to yield, the polished surface of the deformed specimen usually assumed a fog-like appearance. It consisted essentially of small flow figures spread evenly along the gage length. The onset of localized deformation was still recognized as a coalescence of the flow figures, but the visibility of the onset of localized deformation zone and its further expansion stage were much weaker than those exhibited in class A. This faintly appearing localized deformation zone with the typical plastic instability phenomenon as class A is regarded as class C. It has the characteristic of semi-discernible type of plastic instability as shown in Figure 12.

In steel D6A at both strength levels, none of the specimens broke in the usual manner with a shear mode fracture as shown in Figure 9. They all broke in a brittle manner with helixial type of fracture, as described by Ross (15) and demonstrated in Figure 13. The onset of localized deformation zone was still observable, but the extent of its expansion stage was largely reduced. It seemed that the stringer type inclusions found in the longitudinal direction of the specimen had a remarkable effect upon both the total amount of plastic strain and the mode of fracture.

As the fluctuation of the load generally results in a successive increase of the load during expansion of the localized plastic deformation, it is apparent that this manifestation of increasing load can be related to the strain-hardening effects of the steels. Thus, the steels in class A and class C which have displayed a typical fluctuation phenomenon of the load are supposed to experience a higher work-hardening rate or a higher strain-hardening exponent as compared with steels in class B. This conclusion appears in good agreement with experimental results. But, when correlating strain-hardening exponents to the instability phenomena in torsion, the above statement seems inadequate to explain that steels with higher strain-hardening exponents are more susceptible to instability phenomena as compared with steels in class B. This inconsistency can be attributed to the high alloy content permitting the use of higher tempering temperatures for the steels in class B. Because the steels exhibiting a discernible instability as shown in class A are usually tempered at a comparatively low temperature, it is likely that the instability phenomena in torsion are related to the tempering temperature used to attain such high strength level in those steels. As the function of tempering is essentially to reduce the residual stresses set up in quenching, it seems that the incomplete removal of residual stresses has considerable effect on the susceptibility

Figure 11. Class B - Vague Instability (No discernible localized deformation zone was detected in steel H-11 at both strength levels)

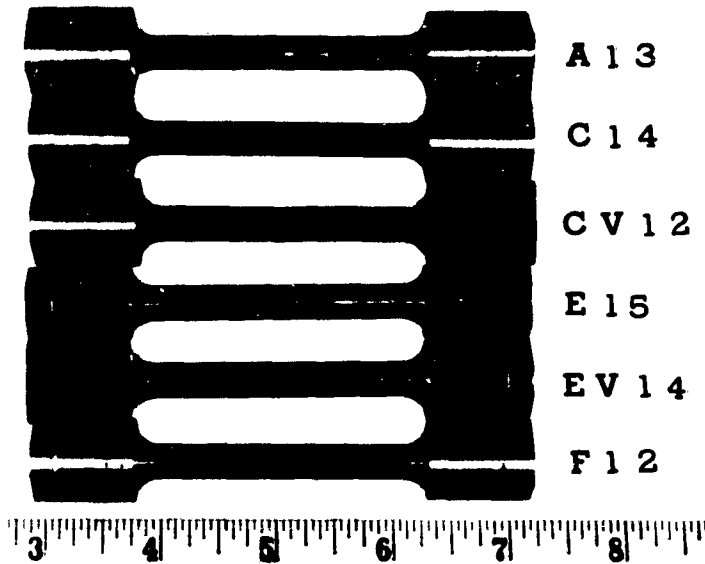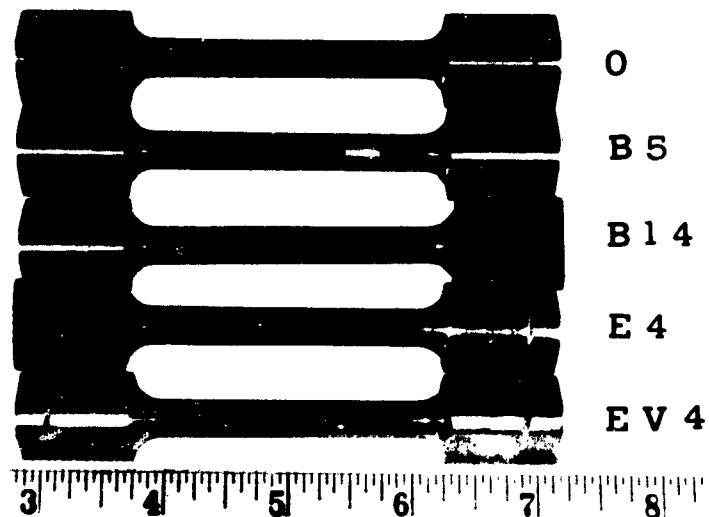Figure 12. Class C - Semi-Discernible Instability Observed in Steel 300M at Both Strength Levels and Mx-2 at High Strength Level
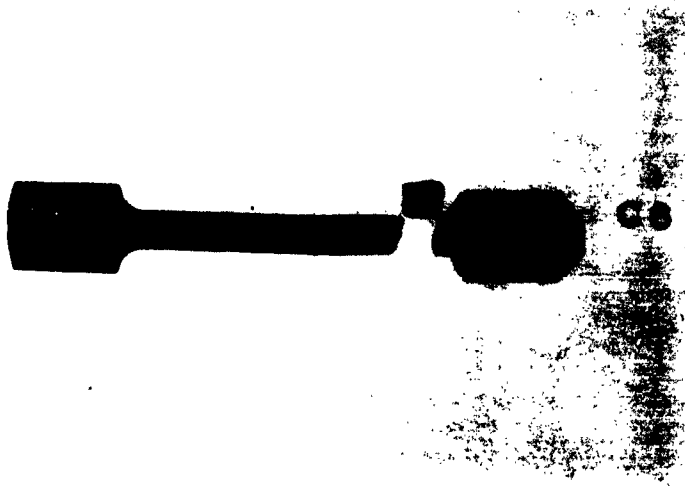
26

Figure 13.   Helical Type of Fracture in Steel
D6AC at High Strength Level

to localized plastic deformation. It seems true that a low tempering temperature favors the instability phenomena in torsion.

A comparison of the instability parameters obtained both in torsion tests was made. The converted shear stress and strain at which tensile instability occurs and the related shear stress-shear strain data in torsion are given in Table VII. As the condition of plastic flow depends mainly on the state of stress, a metal is expected to behave in a more ductile manner in torsion than that in tension (16). This dependency of state of stress on plastic behavior is well demonstrated in Table VII. The plastic strain for the onset of instability in torsion is found to be considerably larger (2-5 times) as compared with those in tension. The stresses at which tensile instabilities occur are also given in the table. These instability stresses were determined by dividing the maximum load with the area obtained when the load started dropping. As it can be seen readily from the table, they are identical to the stresses at maximum load point. But in torsion, instability usually occurs before reaching the maximum torque. The instability stress in torsion is generally 2.8% less than the stress at maximum torque. And also, the instability strain and strain at maximum torque vary considerably as can be seen in Table VII. Thus, the conditions for instability derived basically from maximum load criterion are hardly valid for a metallic bar subjected to torsional loading. In tension, a maximum in the load occurs because of the phenomenon of necking down, and the highly localized deformation is developed under such a circumstance that the rate of increase of stress due to strain hardening becomes gradually smaller than the rate of increase of stress due to the decrease of cross-sectional area. In torsion, experimental results have shown that the localized plastic deformation usually occurs before reaching the maximum torque and the strain at maximum torque is larger than its instability strain except H-11 which exhibited no localized deformation zone. Since there is no geometric effect in torsion such as the necking phenomenon in tension, the maximum torque is reached only by strain-hardening and work-softening effects in the steel. It should be noted also that the maximum shear stress occurred on the surface and the steep strain gradient present in the torsion specimen may contribute to the plastic instability phenomena exhibited in torsion specimen. However, the similarity of instability phenomena occurring in these two types of tests provides a common definition of instability as the change of uniform plastic deformation to localized plastic deformation. It is based upon this condition that the correlation was made. Further correlation analysis of the instability strains was made by plotting the instability strain in torsion versus converted instability strain from tension as given in Figure 14 and Figure 15. Evidently, no definite trend can be discerned from the considerable scattering of points. Results of the correlation analysis have shown that the correlation coefficient for high strength level is 0.318 and its standard deviation is 0.299; for lower strength level the correlation coefficient is 0.549 and its standard deviation is 0.232. It appears that there is no significant correlation between the instability strain in tension and the instability strain in torsion based on the correlation coefficients obtained.

The extent of the expansion of localized deformation zone that a torsion specimen withstands prior to failure can be related to a manifestation of fracture toughness. These values are obtained by the deduction of the

Table VII. Comparison of Tension Instability with Torsion Instability

Steel Desig-nation	Tension Instability						Torsion Instability*						Strength Level
	τ'_{ins}	τ'_{ml}	γ'_{ins}	γ'_t	γ'_{ext}	n	τ_{ins}	τ_{mt}	γ_{ins}	γ_{mt}	γ_t	γ_{ext}	
A6	167,100	167,100	0.087	0.840	0.753	0.064	161,300	165,900	0.098	0.295	0.390	0.292	high
A16	155,900	155,900	0.121	1.030	0.909	0.071	147,900	151,000	0.119	0.570	0.803	0.634	low
B5	169,000	169,000	0.093-0.122	0.835	0.713	0.078	175,800	178,800	0.662	0.680	0.883	0.221	high
B15	149,600	149,600	0.098-0.126	0.957	0.831	0.081	152,700	154,500	0.704	0.980	1.094	0.390	low
C5	169,900	169,900	0.063	0.786	0.723	0.040	155,600	176,300	0.113	0.075	0.159	0.046	high
C15	145,900	145,900	0.098	0.978	0.880	0.052	147,700	151,100	0.136	0.230	0.318	0.182	low
CV5	170,800	170,800	0.077-0.091	0.985	0.908	0.044	175,200	176,300	0.118	0.180	0.196	0.078	high
CV15	148,000	148,000	0.081-0.102	1.080	0.978	0.047	161,400	171,400	0.138	0.650	0.669	0.531	low
D8	169,000	169,000	0.069	0.618	0.549	0.044	166,300	167,900	0.807	0.610	0.807	0	high
D18	149,700	149,700	0.084-0.126	0.815	0.717	0.061	148,400	152,600	0.741	0.640	0.741	0	low
DV8	167,800	167,800	0.074-0.088	0.631	0.557	0.045	174,900	175,500	0.549	0.490	0.549	0	high
DV18	150,000	150,000	0.069-0.126	0.718	0.620	0.056	155,800	156,600	0.547	0.460	0.547		low
E6	167,700	167,700	0.069-0.083	0.772	0.703	0.044	173,000	175,600	0.280	0.420	0.433	0.153	high
E16	149,900	149,900	0.079-0.093	0.800	0.707	0.058	157,100	159,500	0.352	0.470	0.579	0.227	low
EV6	167,900	167,900	0.072-0.086	0.745	0.673	0.046	172,500	176,500	0.263	0.380	0.398	0.135	high
EV16	150,200	150,200	0.078-0.092	0.782	0.690	0.056	156,600	157,000	0.269	0.300	0.415	0.146	low
F5	167,600	167,600	0.107-0.121	1.050	0.929	0.070	174,000	174,800	0.412	0.410	0.448	0.036	high
F15	152,700	152,700	0.095-0.124	1.312	1.188	0.072	157,600	162,300	0.405	0.490	0.626	0.221	low

*Data shown under this column are the averages of the values listed in Tables VI.

Definition of symbols:

n = strain hardening exponent

τ'_{ins} = converted shear stress at which localized plastic flow occurs in tension

τ'_{ml} = converted shear stress at maximum load in tension

γ'_{ins} = converted shear strain at which localized plastic flow occurs in tension

γ'_t = converted total shear strain in tension

γ'_{ext} = (γ'_t − γ'_{ins}), extent of the expansion of localized plastic flow to fracture in tension

τ_{ins} = shear stress at which localized deformation occurs

τ_{mt} = shear stress at maximum torque

γ_{ins} = shear strain at which localized deformation occurs

γ_t = total shear strain

γ_{ext} = (γ_t − γ_{ins}), extent of the expansion of localized plastic flow to fracture in torsion

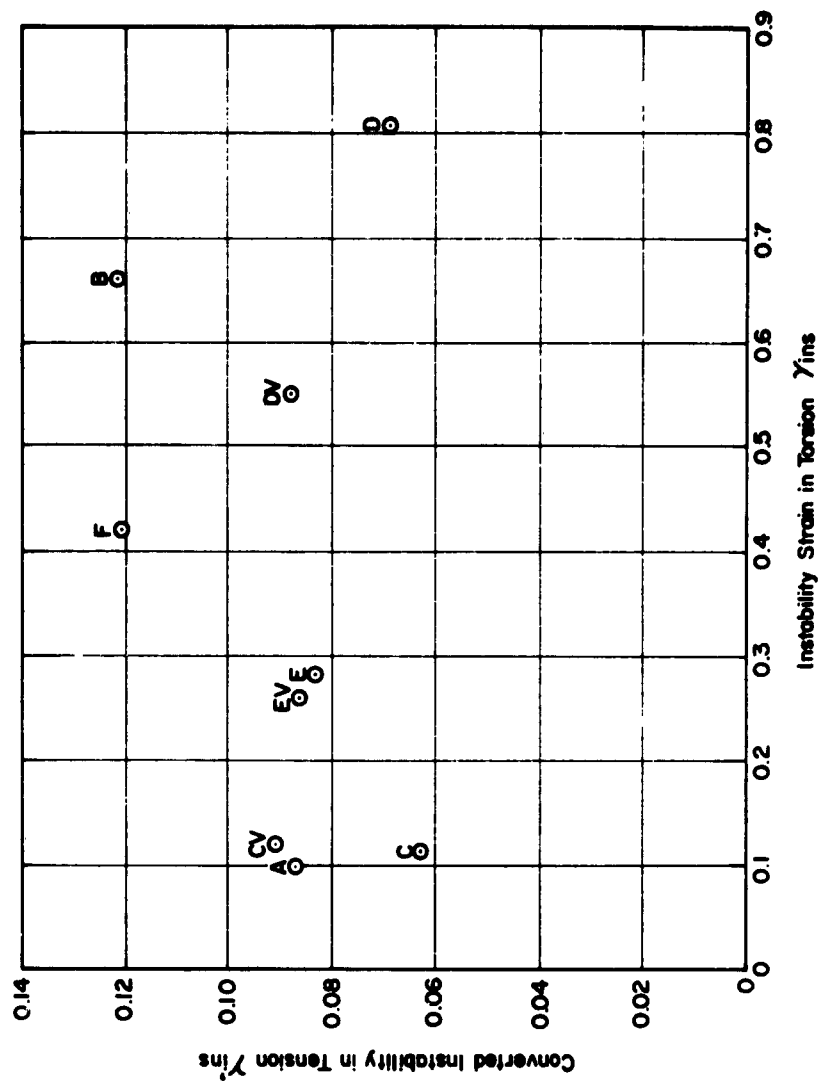γ_{mt} = shear strain at maximum torque

29

Figure 14. Torsional Instability Strain versus Converted Tensile
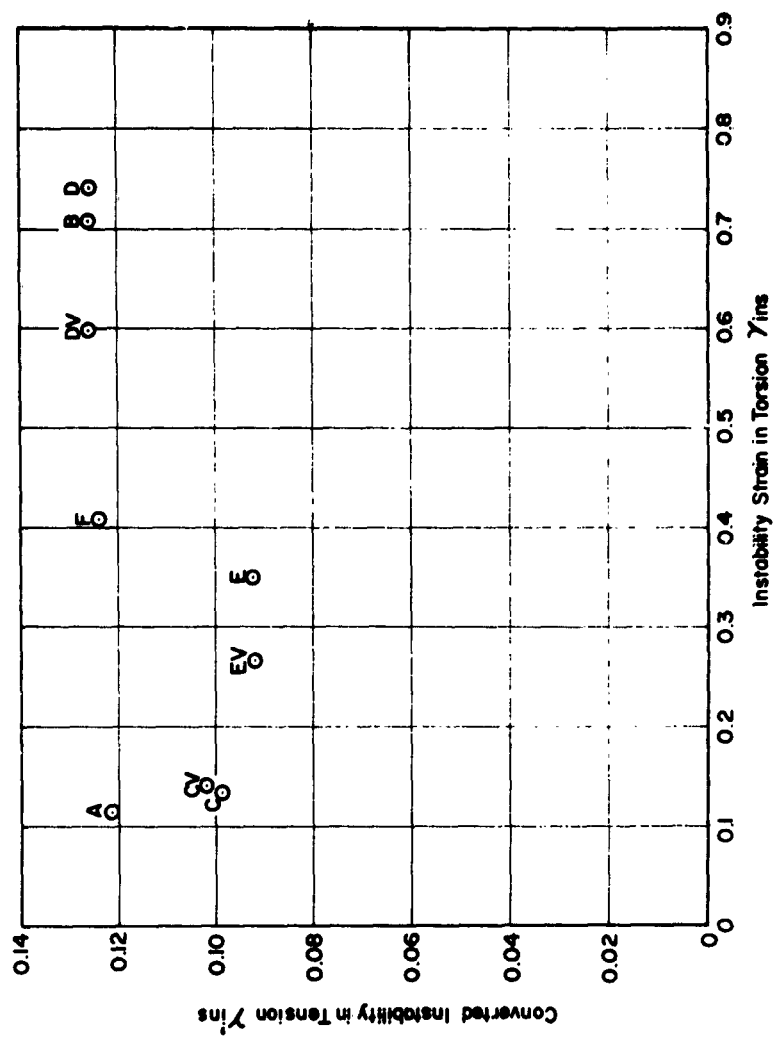Instability Strain at Strength Level of 275,000 psi

Figure 15. Torsional Instability Strain versus Converted Tensile Instability Strain at Strength Level of 250,000 psi

31

instability strains from total plastic strains. Thus the experimental
steels, tempered to a lower strength level which maintains a larger extent
of localized deformation zone, are superior to the same steel heat treated
to the higher strength levels.

The shear strain at onset of localized flow (γ_{ins}) is regarded as
the parameter indicative as the resistance to fracture initiation. The total
ductility (γ_t) is deceptive because beyond γ_{ins}, much of the flow is local-
ized in bands. A measure of the strength of the instability is taken as
$\gamma_t - \gamma_{ins}$; the larger this value, the weaker the instability. These parameters
are listed in Table VIII in decreasing order of γ_{ins} for both strength levels.
The strength of the instability ($\gamma_t - \gamma_{ins}$) do not vary in the same order.
AISI 4340, for example, has the lowest γ_{ins} but the weakest instability. The
effect of lowering the strength level is to increase γ_{ins} and to weaken the
instabilities. The H-11 steel produced no localized flow at these two strength
levels.

5. Photographic Study of Localized
   Deformation in Torsion

Further study of the nature of instability in torsion was made
using surface replica techniques. It involves the use of cellulose acetate
replication tape, which is softened on one side by acetone solvent. The
softened side of the tape is then brought into intimate contact with the
localized deformation zone on the surface of the torsion specimen. After
the solvent has completely evaporated, about 5 seconds, the tape is stripped
off and is ready for microscopic observation, since shadowing is unnecessary.
For best results, one has to locate at a low magnification (15 X) that por-
tion of the replica which is an exact reproduction of the contour of the
specimen surface, and cut off that part of the replica. Next, a drop of
acetone is put on the glass slide and that portion of the replica with the
blank is affixed to the slide. This slide is then observed at high magnifi-
cation.

In each steel at each strength level there are generally four pic-
tures illustrating the particular stage of development of the localized de-
formation zone. The first picture, for example, Figure 16a, shows the onset
of localized plastic deformation. It reveals the highly localized deformation
zone surrounded by the uniformly deformed zones. The zones of localized flow
develop in planes perpendicular to the axis of the specimen and are observed
to expand in the direction of the axis.

The second picture, for example, Figure 16b, represents the expan-
sion stage of the localized deformation zone as strain was increased to a
value between γ_{ins} to γ_t. As plastic strain propagates, flow figures in the
concentrated deformation zone became more random. Slip bands in some pictures
can also be observed.

The third picture, for example, Figure 16c, reveals the propagation
of a crack initiated by the localized plastic flow. The replicas were made
just before the specimen broke. Highly concentrated plastic flow is readily
seen at the tip of the propagated crack which occurs usually at the advancing

Table VIII. Comparison of the Experimental Steels Based upon the Susceptibility to Crack Initiation

Code Name		Steel Name	Resistance to Fracture		
			Initiation γ_{ins} in/in	$\gamma_t - \gamma_{ins}$	Ductility γ_t in/in
D		H-11 (air melted)	0.807	0.0	0.807
DV		H-11 (vacuum melted)	0.549	0.0	0.549
B		300M	0.662	0.221	0.883
F	Strength Level 275,000 psi	Hy-Tuf	0.412	0.036	0.448
E		Mx-2 (single vacuum)	0.280	0.153	0.433
EV		Mx-2 (double vacuum)	0.263	0.135	0.398
CV		D6AC (vacuum melted)	0.118	0.078	0.196
C		D6A (air melted	0.113	0.046	0.159
A		AISI 4340	0.090	0.300	0.390
D		H-11 (air melted)	0.741	0.0	0.741
DV		H-11 (vacuum melted)	0.547	0.0	0.547
B		300M	0.704	0.390	1.094
F	Strength Level 250,000 psi	Hy-Tuf	0.405	0.221	0.626
E		Mx-2 (single vacuum)	0.352	0.227	0.579
EV		Mx-2 (double vacuum)	0.269	0.146	0.415
CV		D6AC (vacuum melted)	0.138	0.531	0.669
C		D6A (air melted)	0.136	0.182	0.318
A		AISI 4340	0.119	0.684	0.803

33

Specimen
Axis
←————

Specimen
Axis
————→

180X
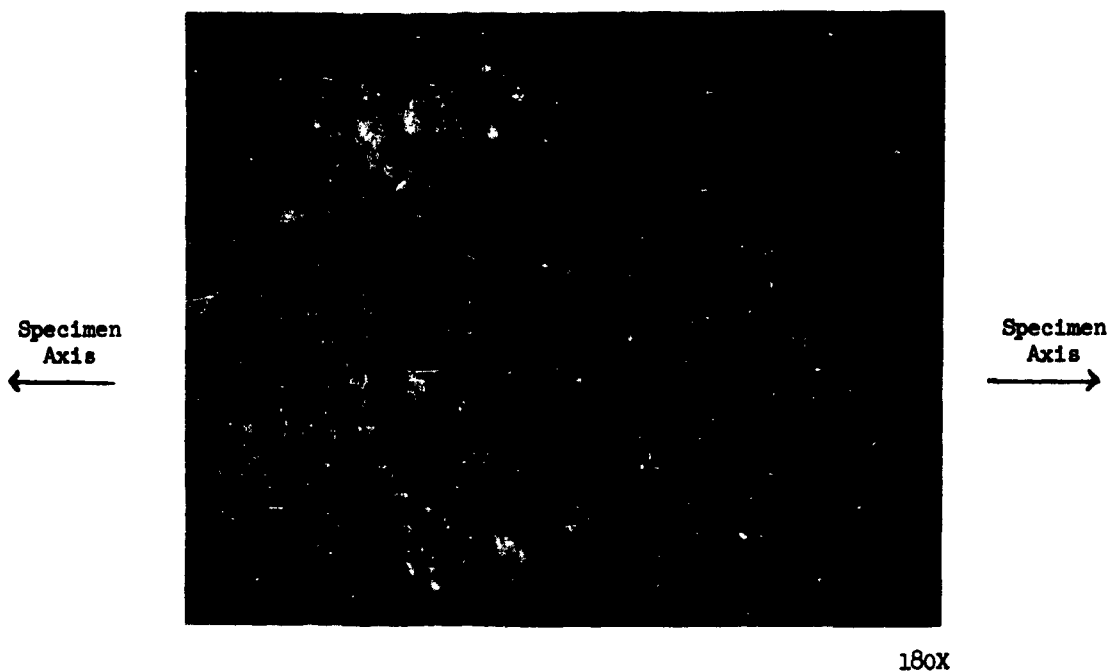
Figure 16a.   The Onset Stage of the Localized Deformation Zone
in Steel 300M at the Strength Level of 275,000 psi

Specimen
Axis
————→

Specimen
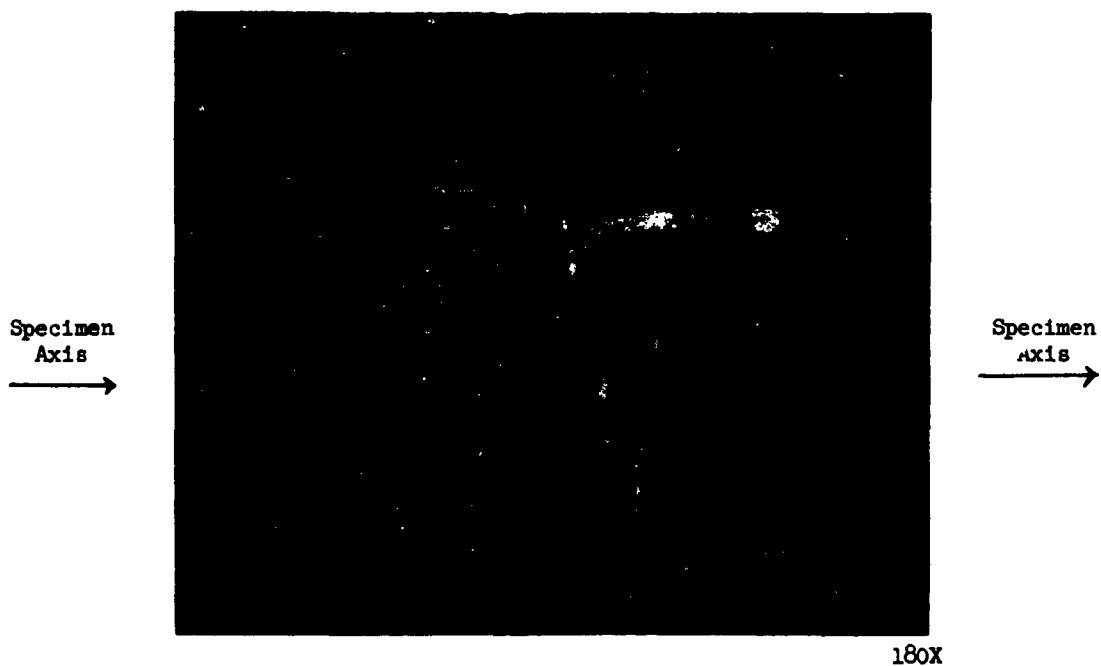Axis
————→

180X

Figure 16b.   The Expansion State of the Localized Plastic
Deformation Zone at Strain Value 0.724

34

Specimen
Axis
←

Specimen
Axis
→

180X

Figure 16c. The Fracture Stage of the Localized
Plastic Flow at Strain Value 0.873

35

front of the localized deformation zone. Besides, the picture also shows the site of intense surface disturbance and the complex slip with the consequent turbulent flow patterns at the tip of the propagated crack. The disturbance took the form of sharply defined corrugations or ridges and grooves. Instead of expansion of the localized deformation zone, the propagation of a running crack under the influence of stored elastic energy occurs during this stage.

6. Conclusions

The classical maximum load criterion for onset of plastic instability in simple tension appears to be invalid for a round steel bar subjected to a torsional loading, because the conditions leading to such a maximum load in these two types of tests are quite different. In tension the maximum load is reached at about the same time as necking begins. It is the geometric effect of necking that produces a maximum load phenomenon. In torsion, no geometric effect like necking which introduces a triaxial state of stress is encountered. The maximum load is reached simply because of the strengthening effects and work softening effects induced by plastic deformation. Experimental results have shown that the plastic strain at which instability occurs in torsion is larger (2-5 times) than the instability strain in tension. This difference may be attributed to the geometric effect of necking produced in tension and the steep stress and strain gradient existing in torsion bars. It seems that the amount of uniform strain prior to instability depends mainly upon the method of loading.

The cause of the exhibition of localized plastic deformation associated with a minor fluctuation of the load is related to structural discontinuity produced either by the variation of chemistry in the steel or the heat treatment employed. The fluctuation of the load observed in the torsion test has revealed that steels with high strain hardening exponents generally are more susceptible to this phenomenon. This indicates that the fluctuation of the load is a manifestation of some strain-hardening characteristics in the experimental steels. Results have also shown that high alloy content permitting the use of high tempering temperatures tends to retard both the plastic instability and load fluctuation phenomenon as seen in Steel H-11. The instability strain in torsion, which can be regarded as the relative ability to withstand ductile crack initiation, is a convenient measure for screening the steels investigated. The relationship of this parameter to other criteria of susceptibility to crack initiation has yet to be established.

C. BEND TESTING

1. Introduction

The torsion testing of the selected steels has provided an indication of the relative susceptibilities of these steels to crack initiation. In order to complete the study of the fracture characteristics of these steels, bend testing of standard Charpy "V" notch bars was undertaken. The objectives of this particular testing program are the measurement of the socalled critical energy release rate, the propagation energy of brittle fracture and, also, the correlation of these quantities with the microstructure.

The experimental apparatus (see Figure 17) being used in this program is similar to that devised by Shimelevich (17). Its basic features are a loading shaft which transmits the force to the specimen and a set of Belleville plate springs which supply energy to the specimen as it deforms. This apparatus is attached to the moving head of a Tinius-Olsen testing machine of 60,000 pound capacity. A more detailed analysis of this apparatus is given later in the report.

This report contains the results of the initial phase of the program. The primary objective of the preliminary experiments has been to determine whether or not meaningful and significant results can be obtained from the type of test employed by Shimelevich. The experimental features of the bend test have been investigated and a satisfactory procedure developed to furnish the desired information. However, before comparative studies of the steels can be made, this method of testing must undergo further critical examination.

2. Development of the Bend Test

The relative susceptibilities of the experimental steels to crack initiation have been investigated by torsion testing. Therefore, one would like to obtain from the bend testing a comparison of the steels with respect to the other stages in the brittle fracture process, namely, acceleration of the slowly growing crack to a certain critical speed and the propagation of this crack at speeds which are a large fraction of the speed of sound (18). The acceleration of a slowly propagating crack may be associated with a certain critical strain energy release rate. Therefore, a comparison of the steels with respect to this stage in the fracture process are made here by comparing their critical strain energy release rates. In addition, the measurement of the energy required for crack propagation should complete the characterization of the selected steels with respect to their propensity toward brittle fracture.

Since this is indeed brittle fracture which is being investigated and moreover only the latter two stages of the phenomenon, all shear elements must be eliminated from the fracture process. The nucleation stage of fracture must be made a non-controlling factor. This was accomplished by the use of a brittle case produced by liquid carburizing in a cyanide bath (19) and the use of distilled water as a crack nucleating agent.

It was found upon continuous loading of case hardened specimens, with or without distilled water, that cracking occurred in the case and was blunted upon entering the matrix. Failure of the specimens would not occur until higher loads were imposed. The failure process consisted, in general, of a slow growth and rapid propagation stage. However, since the energy which must be stored in the system for acceleration of the crack was found to be greater than that which was consumed in propagation of the crack, measurements of the energy of propagation could not be made. The excess energy of the system was expended as vibrations and noise. In other words, the acceleration stage was found to have the dominant energy requirement.
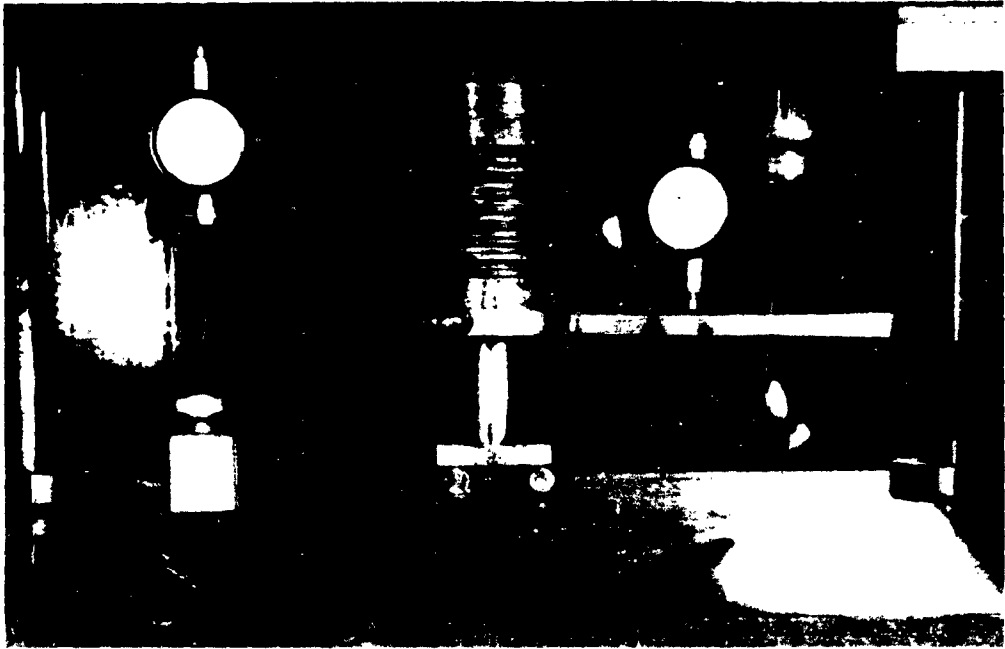
37

Figure 17. Bend Testing Apparatus

The energy stored in the system which consists of specimen, spring and testing machine can be controlled, however, so that only a portion of the stored energy is available in the running stage. The first step which must be taken is to minimize the energy contribution of the testing machine. Obviously, the stiffer the machine and the lower the loads necessary for failure, the lower the energy stored in the machine. The highest load range was used since the movement of the balance head is a minimum for a given load. The use of Belleville plate springs permitted the storing of large amounts of energy at relatively low loads.

Crack formation in the case prior to failure upon continuous loading was utilized as a means of pre-cracking. After pre-cracking by continuous loading, the applied load was relaxed and then set at a prescribed value which was lower than that required for precracking. Distilled water was added to a Scotch tape well fastened about the notch upon reaching the static load. The distilled water greatly aided the slow growth of the initial crack formed by continuous loading. It was found that, using the above testing procedure, loads on the order of 1000 lbs. were sufficient to obtain failure in the experimental steels tested to date (H-11 and Hy-Tuf have not been tested). Measurement of the relative displacement of the balance head and the moving cross-head of the testing machine showed it to be about 0.0025 inch. This value was obtained by reading the dial gage between the moving cross-head and balance head before and after failure, the difference in the readings giving the deformation of the machine. The approximate energy stored in the machine may be calculated as follows:

Work (done on machine) = Strain Energy (of machine)

$$\text{Strain Energy} \cong \tfrac{1}{2} \, (1000) \left(\frac{.0025}{12} \right) \cong 0.1 \text{ ft-lb} \tag{7}$$

The next step which must be taken to permit meaningful measurement of the propagation energy of the specimens is to control the energy released at onset of rapid failure in order that an essentially noiseless, vibrationless fracture be obtained. The ideal test with no excess energy dissipated is obviously experimentally difficult. However, by controlling the position of the restraining nut (see Figure 18) such that complete relaxation of the spring at fracture was not permitted, it was possible to obtain failures with relatively no excess energy. The noise associated with fracture was an insignificant fraction of that of a normal tensile test, and barely audible to the unaided ear.

To summarize, the testing procedure which finally was adopted is as follows. Heat-treated specimens in the form of standard "V" notch charpy bars are loaded continuously either until the clicking associated with the initial crack in the case is heard or it is deemed inadvisable to continue loading due to the increased probability of the occurrence of complete failure. The specimen is unloaded and reloaded at a lower load which is deemed sufficient to cause static failure. Distilled water is added to the well surrounding the notch when the static load is reached. The restraining nut is

Moving Crosshead

Belleville Plate Springs
(Spacing Washers Omitted
for Clarity)

Loading Shaft

A

B

Unadjusted Position of
Nut after a Compression,
A, of the Spring.

Adjusted Position of
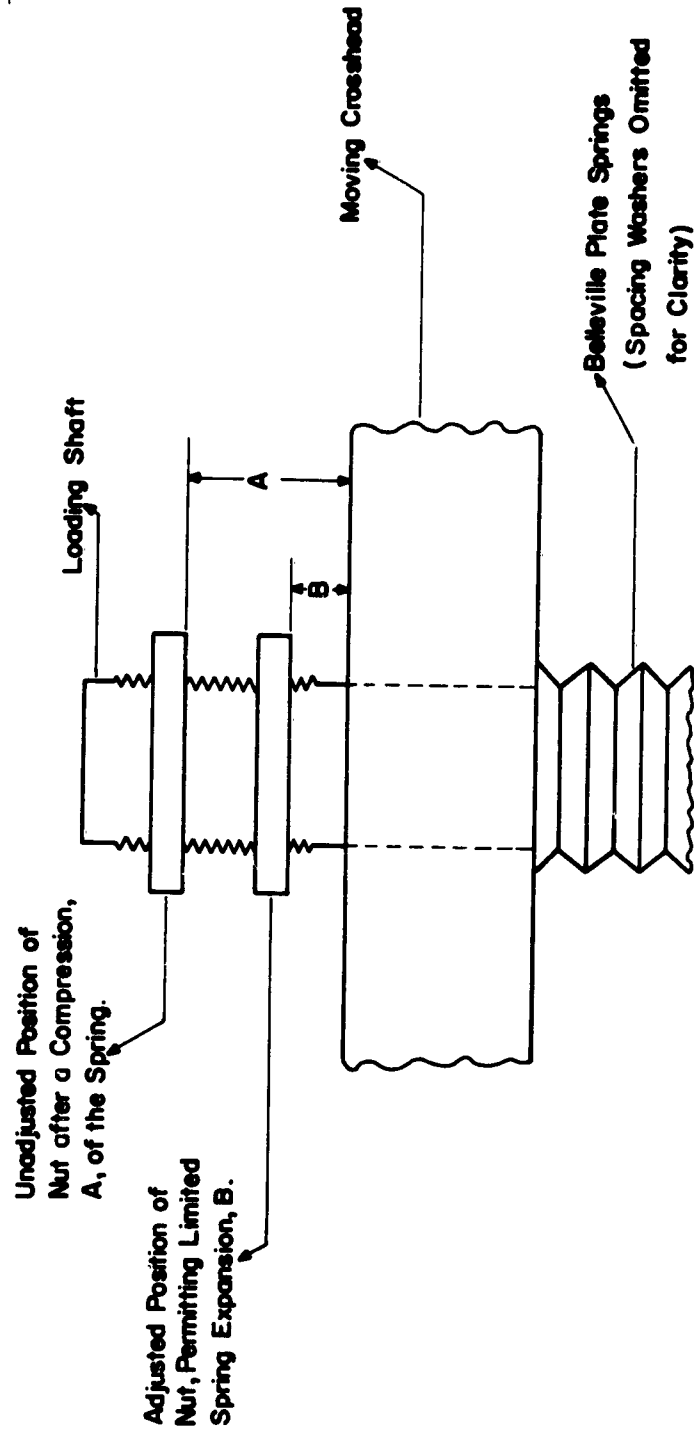Nut, Permitting Limited
Spring Expansion, B.

Figure 18. Schematic Illustration of Control of Energy Released
at Fracture by Position of Restraining Nut

adjusted so that only a slight expansion of the spring can occur upon failure. A series of tests at different loads and using different amounts of available energy is run until a satisfactory test is obtained. The energy expended in the slow growth and rapid propagation stages as well as the critical strain energy release rate are measured by means of dial gage measurements and load measurements.

3. Energy Calculations

The spring used as a source of potential energy for the experimental studied to date has been a series configuration of sixteen Belleville plate springs. The spring constant, K, of this configuration was determined by applying known loads, P, and measuring the associated deflection, x, of the spring system; K is given by the equation

$$K = P/x \tag{8}$$

The potential energy, P.E., stored in the spring system is given by

$$P.E. = \tfrac{1}{2} Kx^2 \tag{9}$$

Neglecting for the present the energy stored in the specimen and considering only the spring system, there appears to be at least two methods of obtaining an estimate of the value of G associated with the onset of rapid fracture. The first method is simply to compute the total stored energy in the spring system prior to rapid fracture and divide this quantity by the heretofore unfractured cross-sectional area; this quantity will be designated by $\bar{G}$. As explained later, an estimate of the unfractured cross-sectional area prior to rapid fracture can be obtained by microscopic examination of the fracture surface. The second method is somewhat more complicated but it does not involve taking an average which is the basis of the first method: this quantity is designated by G_i. It is assumed that the length of the crack propagated during the slow fracture stage is a linear function of the displacement of the spring system at least up to the onset of rapid fracture. This relationship is shown schematically in Figure 19. At the onset of rapid fracture, when the crack increases in length by $d\xi$, the spring system relaxes by an amount dx. The energy given up by the spring system is

$$d(P.E.)_{x=x_{II}} = Kx_{II}dx \tag{10}$$

The energy required by the specimen is
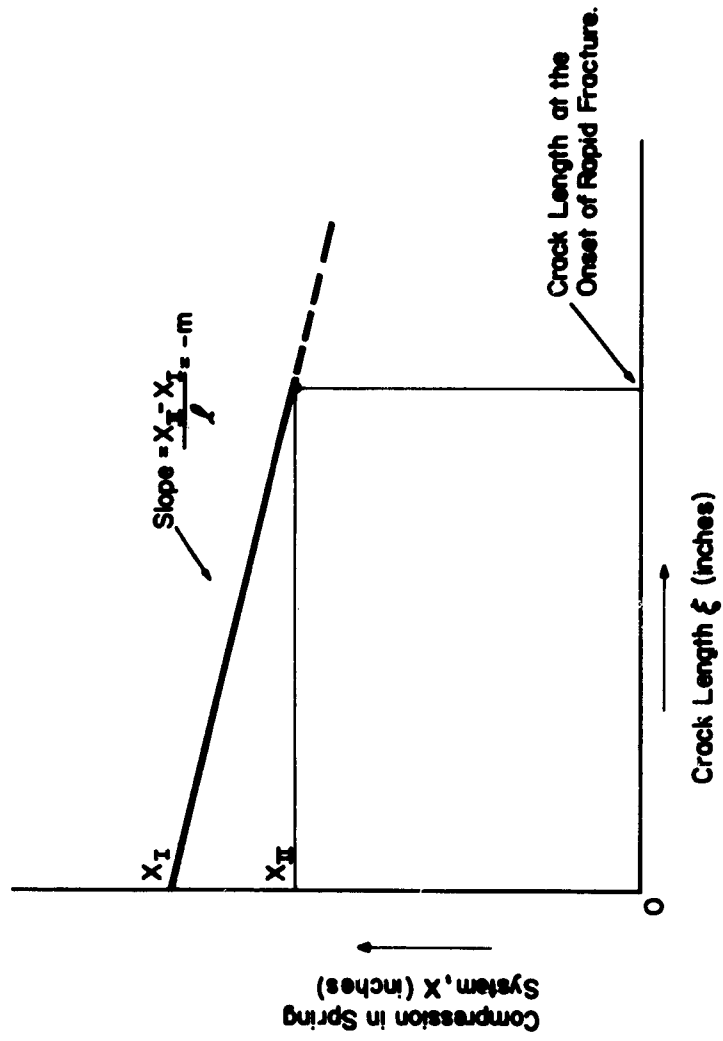
$$dW = G_i 10 d\xi \tag{11}$$

41

Figure 19. Schematic Diagram Illustrating Method of Calculating G_1

42

The factor, 10, is simply the width of the Charpy specimen in millimeters. Equating (10) and (11), there results

$$-KX_{II}dx = G_i 10 d\xi,$$ (12)

the minus sign being present since dx is negative according to the manner in which Figure 19 is drawn. Figure 19 yields the relationship

$$dx = md\xi$$ (13)

Substituting equation (13), equation (12), and solving for G_i there results

$$G_i = \frac{KX_{II}m}{10}$$ (14)

All the quantities on the right side of equation (14) are known for any given specimen.

A third parameter which may be obtained from the experimental data is the propagation energy of rapid fracture, $\overline{G}_p$. $\overline{G}_p$ is defined as the available energy stored in the spring system prior to rapid fracture divided by the total fast-fracture area.

There are at least two methods (20, 21) described in the literature for calculating the value of G associated with the onset of rapid fracture. It must be emphasized that these two methods which will be reviewed below consider only the energy stored in the test specimen and neglect other possible energy sources such as the testing machine. The mathematical treatment according to Wells (20) will be taken up first.

Consider a slow bend specimen of unit thickness deeply notched in the transverse direction leaving a ligament depth, ℓ (Figure 20). Most of the deformation will take place near the ligament. Consequently, an elastic-plastic hinge is formed by the zone of the ligament which is attached to almost rigid arms. Wells further states: "If the bend angle is constant as ℓ is reduced by fast fracture, it then follows that the reaction moment, M, through geometrical similarity, is proportional to ℓ^2 (again whether plastic or elastic) for constant bend angle. The stored energy, W, for any ligament depth, ℓ, is then given by

$$W = \frac{M_0 \Theta \ell^2}{2\ell_0^2}$$ (15)
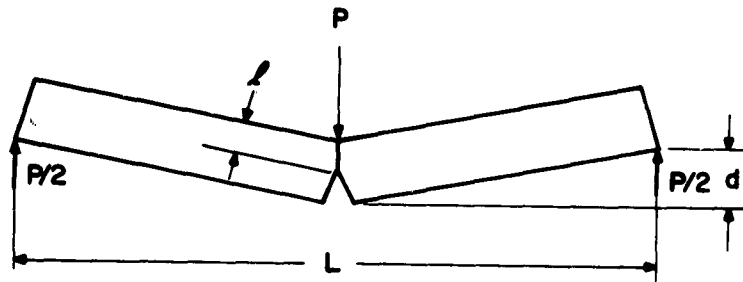
P = Load Applied by Tensile Machine.
L = Loading Span.
ℓ = Ligament Depth.
d = Vertical Deflection of Specimen.

Figure 20. Model According to Wells for Calculating Rate
of Energy Release in the Propagation of a Crack

where M_0 is the value of M when $\ell = \ell_0$. Under the conditions of measurement θ is the bend angle of release when M_0 is removed in an identical specimen which does not fracture."

Continuing with Well's treatment, since the area which has not yet fractured, A, equals the product of ℓ and the thickness, t, where t = 1 mm the following is also true.

$$A = t\ell = \ell \qquad (16)$$

$$dA = d\ell \qquad (17)$$

On differentiating (16) with respect to ℓ, there results

$$\frac{\partial W}{\partial \ell} = \frac{M_0 \theta \ell}{\ell_0^2} . \qquad (18)$$

When the bar first fractures, $\ell = \ell_0$. Therefore, the energy release rate at the onset of rapid fracture is given by

$$\left(\frac{\partial W}{\partial \ell} \right)_{crit} = \left(\frac{\partial W}{\partial A} \right)_{crit} = \frac{M_0 \theta}{\ell_0} \qquad (19)$$

where $(\partial W/\partial A)_{crit}$ is equal to the quantity, G_1, defined above, but, again, it is based only on the energy stored in the specimen.

The second method of calculating the critical value of G is given by Winne and Wundt (21). The quantity, G, is given by

$$G^2 = \frac{(1-v^2) \sigma_n^2 \, h \, f(c/d)}{E} \qquad (20)$$

where

$$\sigma_n = \frac{6M}{h^2}$$

v = Poisson's ratio

M = bending moment at the notched section per unit beam width

45

C = notch depth

h = unnotched thickness,

d = specimen thickness at unnotched position

E = Young's modulus

Evaluating this expression for the experimental system of loading, specimen geometry (standard "v" notch Charpy bars were used), and materials, one obtains

$$G = 4.36 \times 10^{-6}(L^2/h^3)f(c/d) \text{ ft·lb/mm}^2, \tag{21}$$

where L is in lb., h in mm., and $f(c/d)$ is found in Figure 16 of the underated reference.

One can estimate the energy stored in the bar initially in the manner indicated by Wells by putting appropriate measured quantities in the expression:

$$U_{specimen} = \frac{P\theta}{2} = \frac{P}{2} \cdot \frac{L}{2} \cdot \frac{2d}{L} \cdot \frac{1}{2} = \frac{Pd}{4} \tag{22}$$

where

P = load

d = deflection of the specimen in the vertical direction

L = distance between points of support.

For a typical specimen,

$$U_{specimen} = \frac{(1000 \text{ lb})(.005")}{4 \times 12} \text{ ft·lb}$$

$$\approx 0.1 \text{ ft·lb.}$$

This can be seen to be relatively insignificant in comparison to the energy contributions of the spring.

A comparison of the various energy release rates considered above is given in Table IX for three specimens for which complete data are available.

Table IX. Comparison of the Energy Release Rates (ft.lb/in²)
Computed According to the Methods Outlined in the Text

Specimen	Propagation Energy of Rapid Fracture, $\bar{G}_p$	Propagation Energy of Slow Fracture	Energy Release Rate at the Onset of Rapid Fracture, G_1	Acceleration Energy of Rapid Fracture, $\bar{G}$	Well's Release Rate at the Onset of Rapid Fracture, $(\partial w/\partial A)_{crit}$	Winnie and Wundt's Energy Release Rate at the Onset of Rapid Fracture
D6AC 275,000 psi	0.0057	0.0057	0.0052	0.098	0.0058	0.052
D6AC 250,000 psi	0.0031	0.0099	0.0098	0.118	0.0031	0.070
D6AC 250,000 psi	0.0030	0.0082	0.0080	0.113		0.049

The value of $(\partial w/\partial A)_{crit}$ computed from equation (19) has been divided by 2 in order that the energy release rate will be that for each unit of fast-fracture area. The data reveal the following facts:

1. As has often been cited, the propagation energy associated with slow fracture is greater than that for fast fracture (columns 2 and 3, Table IX). The energy absorption in fast propagation seems to vary little.

2. There seems to be no agreement among the four methods of determining the critical energy release_rate at onset of rapid fracture. The G_i and $\bar{G}$ values at least differentiate between the two strength levels tested. Too few data are available to draw firm conclusions. The methods also must be evaluated as to their ability to differentiate among different steels.

If one wishes to take into account the energy contributions of the spring system and the specimen to the fracture process, one would obviously consider adding, for example, G_i and Well's $(\partial w/\partial A)_{crit}$.

At present, it is believed that the results obtained from the type of test described above should be viewed with some caution. As further experience with this test is acquired, the significance of the results should become apparent. An obvious problem which must be probed is whether or not a stress criterion may be involved in the fracture process. This problem can be attacked with this test since it is possible to store a given amount of energy in the spring system at different loads by varying the spring constant. Other possible criteria for acceleration may be a critical load or a critical notch depth. It is also possible that there is no clear cut phenomenological criterion, but that the critical condition may reside in the details of the microstructure.

4. Comparison of Appearance
of Fracture Surfaces

It was found that the appearance of the fracture surfaces is dependent on several experimental variables. A variation was found between specimens of the same steel at the two strength levels, and also between air and vacuum melted heats of the same steel. Moreover, the different experimental steels had varying nature of fracture surfaces, and these differences were subject to modulation by varying the conditions of test, notably the case depth, the amount of available energy and rate of loading. The appearance of the fracture surfaces is indicative of the mode of the fracture process, and should permit correlation of microstructure with the nature of the path taken for fracture. For a more complete analysis of the variation in fracture mode, high magnification , light microscopic, and electron microscopic fractographic analysis would be a useful supplement to the essentially

48

macroscopic study made. However, certain tentative conclusions are drawn based on the observations made.

In general, the first stage, or slow growth stage, of the fracture process has a relatively rough, shiny fracture surface in comparison to the final rapid propagation stage. It is found further that the flatness of both stages is very susceptible to experimental variables. Upon comparison of Figure 21, which depicts MX-2 at 275,000 psi, and Figure 22, which depicts D6AC at 275,000 psi, it is seen that they are in essential agreement. However, the former is somewhat flatter over-all and the demarcation line between the two stages is much more evident that in the latter. If one now considers Figure 23, D6 at 275,000 psi, one observes little difference in the rapid propagation stage, but the slow growth stage has a rougher surface with river-like patterns and hills and valleys evident. Figure 24 depicts the vacuum melted steel, D6AC, at the lower strength level. Again the fracture surfaces are rougher, with irregularities in both stages, a large river pattern is evident in the fast propagation stage. Figure 25 deals with the air melted steel, D6, at 250,000 psi. Both fracture segments are very irregular in this specimen. The fracture process appears to be very discontinuous in the first stage and its extent appears to be very irregular, the selection of the demarcation line between the two stages is quite difficult in some areas.

Figure 26, which deals with 300M at 275,000 psi, is intermediate between Figures 21 and 22. Figure 27, MX-2 at 250,000 psi, is also only slightly different from Figure 21. Of the steels studied to date, the effect of the strength level on the fracture surface has been less significant for AISI 4340, 300M, and MX-2 than for D6 and D6AC. No appreciable differences were seen between MX-2 single and double melted. However, steels AISI 4340 and 300M have only been studied to a very limited extent and decisive conclusions are not possible at the present time.

It was found that by varying the conditions of test only the slow stage or the rapid stage of fracture could be obtained to the exclusion of the other mode. The appearance of the D fracture surface of a specimen of 300M at 275,000 psi broken upon continuous loading is seen in Figure 28. This specimen had no evident slow growth stage in its failure, and the fracture is seen to be the same throughout and quite flat and smooth. Figure 29, on the other hand, shows the fracture surface of D6AC at 250,000 psi. This specimen broke continuously over a period of a few minutes with no rapid fracture stage. The restraining nut was tightened down so that the release of energy from the spring was severely limited in this case. Thus, because of the small amount of available energy, acceleration of the crack was not accomplished. This fracture surface is seen to be very irregular with much evidence of discontinuous fracture.

In discussing the mode of failure observed, and in making micro-structural correlations, it must be remembered that in all cases the first crack was present (in the case of pre-cracking), or in the material altered to greatly lower the difficulty of its formation (the carburized case). The slow growth of the crack occurs by the discontinuous movement of the crack front. The crack grows until it is stopped due to changing stress or material

Figure 21. MX-2, Double-Melted, 275,000 psi. The Slow and Fast Fracture Areas are Clearly Discernible (12X)
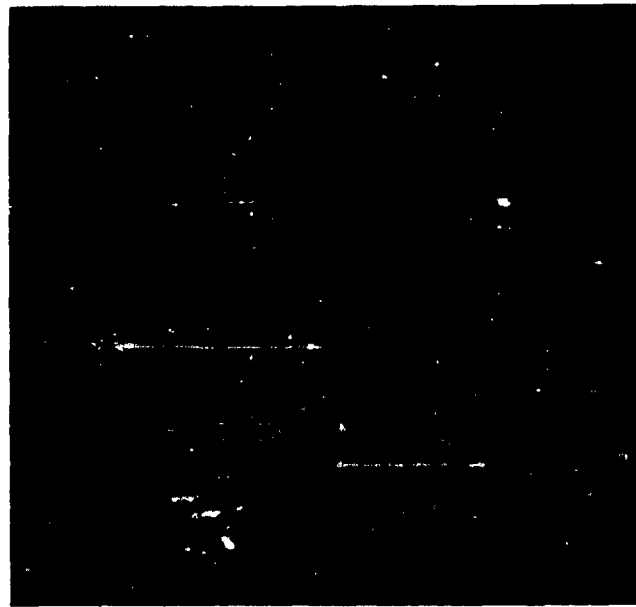

Figure 22. D6AC, 275,000 psi. Two Stages of Fracture (12X)

Figure 23. D6, 275,000 psi. Irregular Surface Features
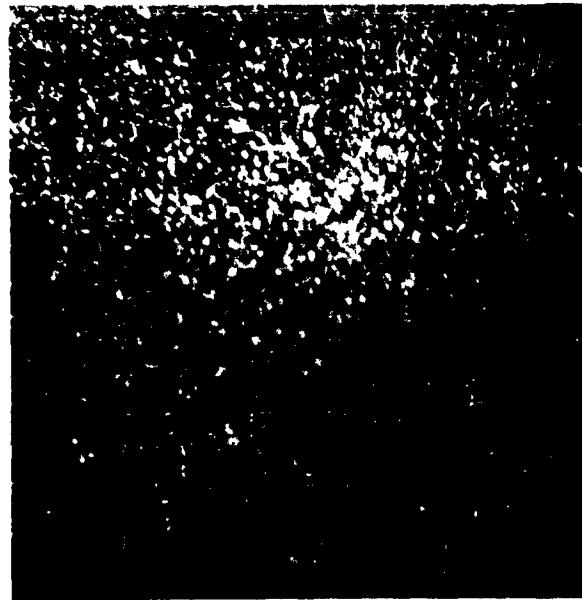Are Seen in the Slow Growth Stage (12X)

Figure 24. D6AC, 250,000 psi. River Pattern
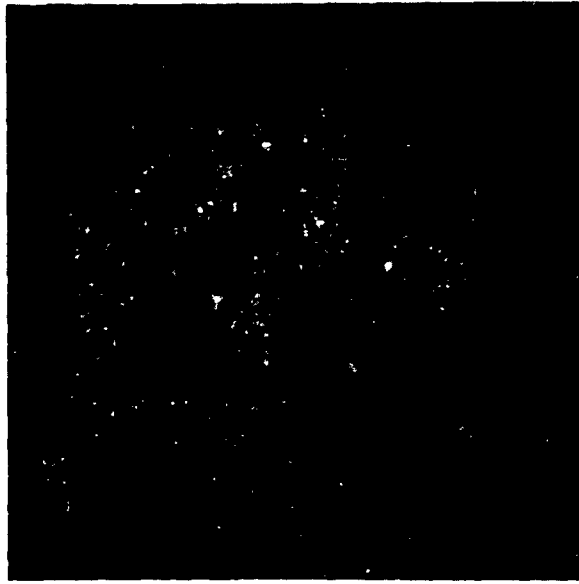is Seen in Rapid Propagation Stage (12X)

Figure 25. D6, 250,000 psi. Very Irregular Surfaces
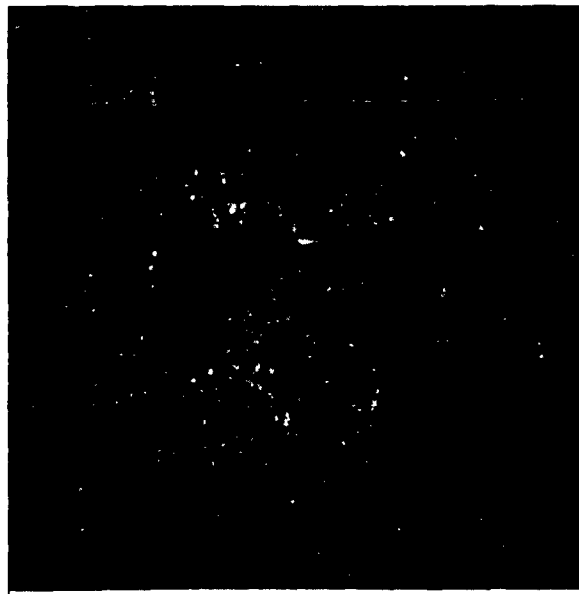are Seen in Both Fracture Segments (12X)

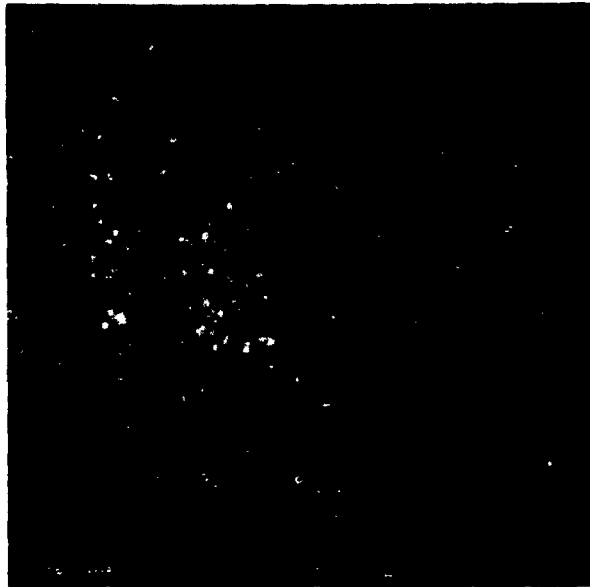Figure 26. 300M, 275,000 psi. Intermediate in Appearance (12X)

52

Figure 27. MX-2, Double-Melted, 250,000 psi. Essentially
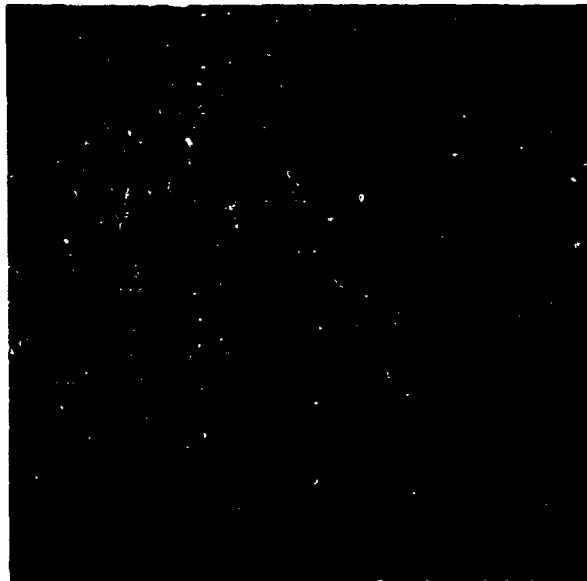Same Appearance as at Higher Strength Level (12X)

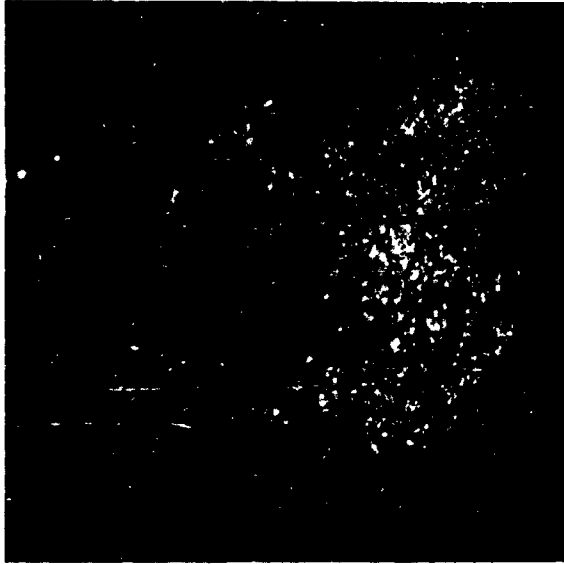Figure 28. 300M, 275,000 psi. Fast Fracture Only (12X)

Figure 29. D6AC, 250,000 psi. No Rapid Fracture
Stage, Very Irregular Fracture Surface (12X)

conditions. If the material is quite uniform with respect to ductility, we would expect that as conditions changed, e.g. due to the corrosive effect of distilled water in our case, such that continued growth was favored, the crack front would move ahead uniformly in the direction of the applied stress field. However, if brittle areas are present, as a result of inclusions or "500°F" embrittlement for example, the crack might grow in a discontinuous manner. Those areas more susceptible to fracture being consumed while the more resistant areas remain intact, or are encircled. This is thought to explain the bizarre appearance of the fracture surfaces found in the slow fracture stages of some specimens, notably D6.

To obtain the fast fracture stage, the slowly growing crack must be accelerated. If we consider an inhomogeneous material with weak areas, it would seem that since crack growth is easier in these areas acceleration would also be more easily accomplished in these areas. However, if we consider an arrested crack front, the weak areas might serve as safety valves which relieve the stress field build-up before it becomes sufficient for acceleration. The weak areas yield at low stresses and hence the critical value for acceleration may not be obtained until later or not at all. This is thought to explain the ability to eliminate the fast stage in steels D6A and D6AC, which it has not been possible to do so with MX-2. However, this is not to say it could not be done with MX-2, but only that MX-2 is more resistant to this manipulation. Above all, it should be borne in mind that a structure has failed whether by the slow or fast fracture processes. The chance of blunting an accelerated crack is much less than that of blunting a slowly growing crack, but the slowly growing crack, in a non-homogeneous material, can proceed to failure without the energy requirements imposed by acceleration of the crack.

IV.   STRUCTURAL STUDIES

A.   INTRODUCTION

In order to explain the mechanical behavior of the experimental steels, certain microstructural investigations were undertaken, and a determination of the relative inclusion content of the steels was made. The morphology of the carbide precipitates was studied by surface and extraction replica electron microscopy. The composition of the carbides was determined by selected area transmission electron diffraction analysis of the extraction replicas. An attempt was made to obtain mean free distance and volume fraction values for the microstructures studied. However, experimental difficulties mitigated against the attainment of reliable data.

Although the analysis of the microstructures is incomplete with respect to matrix properties and the presence of retained austenite, certain observations were made which, it is believed, help to explain the torsional properties, and the fracture characteristics of the steels studied. For example, the steels with larger amounts of inclusions appear to be more susceptible to the onset of plastic instability, as would be expected. Also, preliminary results appear to indicate that the inclusion content affects the process of

failure in static bend testing. However, sufficient bend testing to establish this observation has not as yet been conducted.

B. INCLUSION RATING

Longitudinal sections of the various steel bars from which the test specimens were prepared were polished and examined under the microscope at 100 X. The inclusion rating was accomplished by comparing the steels with standard areas found in the SAE Handbook, 1962, pp. 106-110. The results are given in Table X. The values reported are, in all cases, averages of the worst areas found in the section. The greater cleanliness of the vacuum melted steels is evident.

C. ELECTRON MICROSCOPY

The techniques of electron metallography used were those of surface and extraction replication and selected area electron diffraction analysis of extraction replicas. The surface replicas were two-stage negative replicas. The initial surface replicas were made of 1% collodion in amyl acetate. The final replicas were gadolinium-shadowed. Carbon replicas were prepared from the collodion impressions. The extraction replicas were direct carbon replicas prepared by double etching of the specimens in Nital-Zephiran Chloride. The electron diffraction analysis was made using extraction replicas freshly prepared as described above. A detailed listing of the diffraction data with sample calculations has been given in an earlier report (2d).

Initially, it was intended to analyze the various microstructures by means of quantitative metallography. The quantities of interest were the volume fraction and mean free distance between particles. However, a magnification of the true volume fraction and reduction in the true mean free distance results from the effect of etching. This etching effect is particularly troublesome for the small, finely dispersed particles encountered in the microstructures of the experimental steels. It was attempted to apply a correction factor (23, 24) in order to alleviate this difficulty. However, this correction term is itself subject to an etching effect and caused over-correction of the data. Since the differences in the quantitative parameters of the experimental steels are undoubtedly small, it was felt that sufficient technical accuracy was not possible to permit useful comparisons. A detailed account of this area has been made previously (22).

Certain of the experimental steels studied were found to be basically identical from a microstructural viewpoint. These low alloy steels, AISI 4340, 300M, D6, D6AC, MX-2 single- and double-melted, all contain about 0.40% C and differ essentially only in their alloying elements. Certain variations were observed in their microstructures, however. The remaining steels, Hy-Tuf and H-11, air- and vacuum-melted, were quite different from each other and the previous steels. Hy-Tuf contains only a moderate amount of carbon, 0.25%, and H-11 is a high alloy hot work die steel (5% Cr).

Table X. Inclusion Ratings of the Experimental Steels

Steel	Oxide Rating	Silicate Rating*
AISI 4340	2	2
300M	2½	
D6	3½	
D6AC	< 1	
H-11 (air)	1	
H-11 (vac.)	< 1	
MX-2 (single VAM)	1	
MX-2 (double VAM)	< 1	
Hy-Tuf	2	1½

*Based on SAE Standard Inclusion Rating Charts

AISI 4340 and the other low alloy steels containing about 0.40% C all appear to be effected to some extent by "500°F embrittlement" at the 250,000 psi strength level. This is based on the criteria generally accepted, namely, the transition of the carbide precipitate from epsilon carbide to cementite (25), and the appearance of platelet cementite early in the third stage of tempering (26). It must be remembered that recent investigations with high purity special melted steels (27) have cast doubt on the completeness of the above criteria and there is no solely microstructural means for determining the degree of the embrittlement. The properties of the matrix, as effected by various trace elements (27) and in general, may indeed have a greater role in "500°F embrittlement" than is commonly thought. This is certainly an area requiring further investigation.

The above steels at the higher strength level (275,000 psi T.S.) consist essentially of a matrix of low-carbon martensite with epsilon carbide precipitates. Certain amounts of cementite have been detected visually and by diffraction in some of the steels, however, suggesting that "500°F embrittlement" may be somewhat in play here also. Hy-Tuf at both strength levels had a microstructure suggestive of epsilon carbide in martensite and diffraction analysis indicated the presence of epsilon carbide. However, due to the difficulty of extracting sufficient quantities of carbides for analysis, positive identification of their composition is difficult. The carbon content of this steel (0.25% C) is right at the minimum amount generally accepted as necessary for the transitory stage of epsilon carbide precipitation. H-11 at both strength levels contained several different carbides. Again positive identification of their exact composition was difficult. The difficulties here were that several possible carbides have about the same "d" spacings and the inability to clearly resolve some of the more intense, closely spaced reflections. However, the presence of alloy carbides in addition to Fe_3C is quite evident. This is as would be expected since a secondary hardening reaction is reported in this steel at about 950°F (28). Moreover, an embrittlement related to the early stages of secondary hardening is well known in such steels as this, and may play a certain role in the experimental steels. The steels shall now be considered in detail at the two strength levels.

57

1. AISI 4340

    Both ε-carbide and Fe₃C were identified by electron diffraction analysis at the 275,000 psi strength level. This duplex structure is exemplified in Figure 30. Both carbides were also identified at the lower strength level; however, Fe₃C was by far the predominant carbide present. Some rather coarse cementite platelets are seen in Figure 31. Figure 32 depicts an interesting configuration of parallel carbide platelets.

    Based upon the above evidence, it is proposed that this alloy is in an embrittled condition. The predominant carbide in the microstructure is seen to be changing from ε-carbide to Fe₃C. Platelet cementite has been observed at both strength levels. In the literature (25, 26), it has been proposed that "500°F embrittlement" is in some way related to the solution of ε-carbide and precipitation of cementite early in the third stage of tempering. The presence of platelet cementite has also been considered to be indicative of this embrittlement. Therefore, based upon microstructural evidence, this steel is seen to be embrittled at both strength levels.

    The closely spaced, parallel cementite platelets are also of interest from a point of view of embrittlement, and, similarly, of the onset of instability. A dislocation pile-up at the first platelet of the colony would intensify the stress on the other side of the platelet. However, plastic flow of the matrix on the other side of the platelet is restrained due to the close proximity of the next, parallel platelet and the build-up of stress procedure is repeated. Moreover, the matrix surrounding the colony of platelets would be expected to be relatively low in cohesive strength because of the relatively low carbon content due to the large amount of precipitation involved in the adjacent cementite colony. Thus, it seems conceivable that a micro-crack the size of the entire cementite colony might be formed under proper conditions, and initiate failure, or unstable plastic flow.

    2. D6 and D6AC

    The microstructures of these steel's D6 and D6AC, were not found to differ significantly, aside from the standpoint of inclusion content. Two main observations on them are that basically they are similar in appearance to AISI 4340 and that appreciable quantities of undissolved carbides are present. The identification of some carbides as undissolved carbides is based upon the relatively large size and rounded appearance of these carbides, in comparison to the smaller, more elongated, platelike precipitated carbides. Large undissolved carbides and finer, Widmonstätten type carbides are seen in Figure 33, depicting D6 at 275,000 psi Figures 34 and 35 depict D6AC at 275,000 psi. Epsilon carbide and cementite were both identified by electron diffraction.

    Figure 36 shows the microstructure of D6 at 250,000 psi, and Figure 37, D6AC at the lower strength level. Electron diffraction analysis revealed only Fe₃C at this strength level. However, trace quantities of ε-carbide could well be found by more detailed analysis.

Figure 30. AISI 4340, 275,000 psi, Surface Replica, 21,000 X
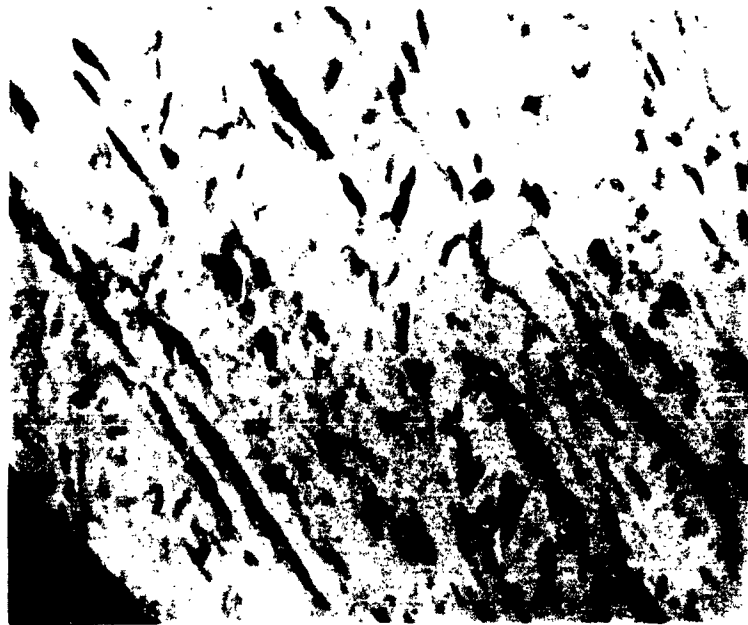Duplex Structure of Fe_3C and ϵ-carbide

Figure 31. AISI 4340, 250,000 psi, Extraction Replica, 35,000 X
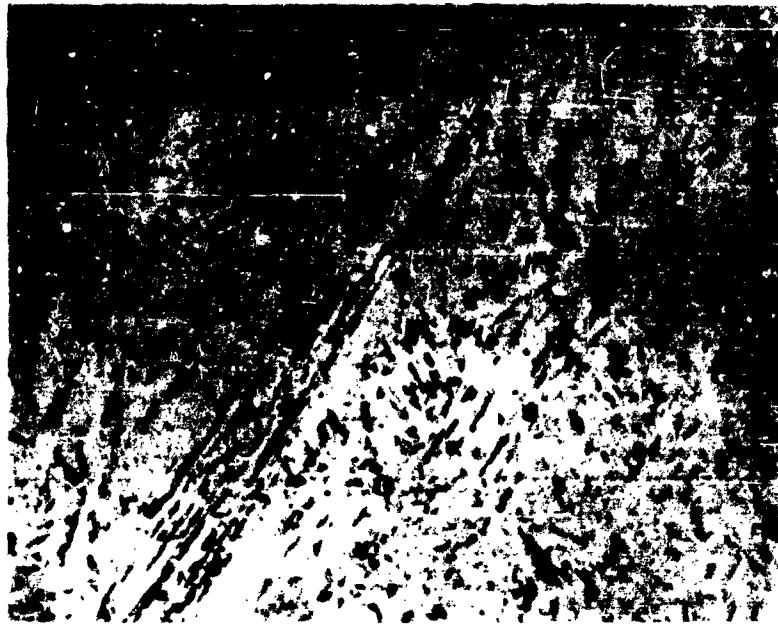Coarse Carbide Platelets are Seen

Figure 32. AISI 4340, 250,000 psi, Extraction Replica, 14,000 X
Parallel Carbide Platelets are Seen

Figure 33. D6A (air), 275,000 psi, Extraction Replica, 14,000 X
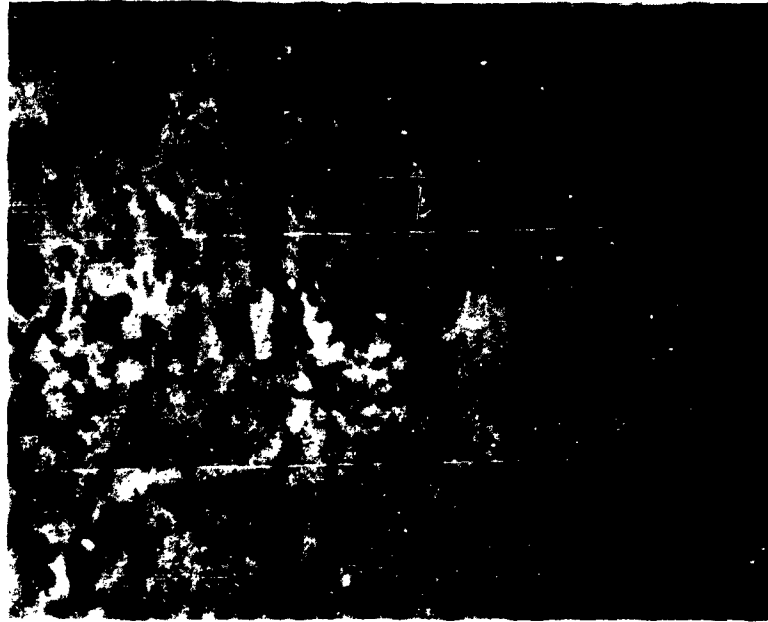Large Undissolved Carbides and Fine Widmanstatten Carbides

Figure 34. D6AC (vac.), 275,000 psi, Extraction Replica, 35,000 X
Widmanstätten Carbides and Rounded Undissolved Carbides

Figure 35. D6AC (vac.), 275,000 psi, Extraction Replica, 35,000 X
Rounded Undissolved Carbides

61

Figure 36. D6 (air), 250,000 psi, Extraction Replica, 14,000 X
Parallel Carbide Platelets

Figure 37. D6AC (vac.), 250,000 psi, Surface Replica, 35,000 X
Long Carbide Films

These alloys are proposed to be embrittled for reasons previously cited for AISI 4340. They appear to be farther progressed into the third stage of tempering, and hence should be more ductile due to the greater and more uniform depletion of carbon from the matrix. However, the presence of undissolved carbides complicates the picture. Their effect on over-all ductility is not understood. They would certainly not be expected to be beneficial. Moreover, since these undissolved carbides are present, it would seem that a higher austenitizing temperature should effect an increase in ductility. This was, indeed, found my ManLabs (29). This whole analysis is complicated by the further findings of ManLabs that the ductility of this steel (D6AC) varies anomalously from one heat to the next. This serves to point out the relatively incomplete nature of purely microstructural analysis of the kind undertaken. Certain conditions of carbide composition and morphology have been revealed; however, this is but a part of the complete classification of the brittle fracture susceptibilities of the steels studied.

3. Hy-Tuf

The microstructure of this steel at the 275,000 psi strength level is seen in Figure 38. Very fine precipitates as well as elongated films are seen. Electron diffraction analysis of extraction replicas indicated the presence of ϵ-carbide, but due to the nature of the carbides (i.e., it was very difficult to extract the extended carbides, the fine carbides were quite small, and both types oxidized quite readily), it was impossible to obtain sufficient reflections for conclusive analysis. Figures 39 and 40 deal with this steel at the lower strength level. Epsilon carbide was again the only carbide identified, but the previously discussed limitations to conclusive determination are still present.

This steel at the tempering temperature employed to obtain the 275,000 psi strength level appears to be in an early stage of tempering, characterized by epsilon carbides and low carbon martensite matrix.

4. 300M

The primary observation made on this alloy is that the carbide precipitates, particularly at the lower strength level are finer and tend to be less elongated than those of AISI 4340, D6 and D6AC. Also, no parallel platelet colonies were observed. The additional observation, however, is made that carbide precipitation appears to be concentrated in certain areas and relatively light in other areas at the lower strength level. This would be expected to a certain extent due to the high magnifications used.

Figures 41 and 42 depict the microstructure of this s̲ ̲ ̲ ̲ ̲ higher strength level. Epsilon carbide was revealed as the preꜱꜱ ꜱ ̲ ꜱe at this strength level by electron diffraction. The presence of cementite was also indicated. Figures 43 and 44 deal with this steel at 250,000 psi. The concentration of precipitation in certain areas with bare areas adjacent can be seen. Cementite was the only carbide identified at this strength level.
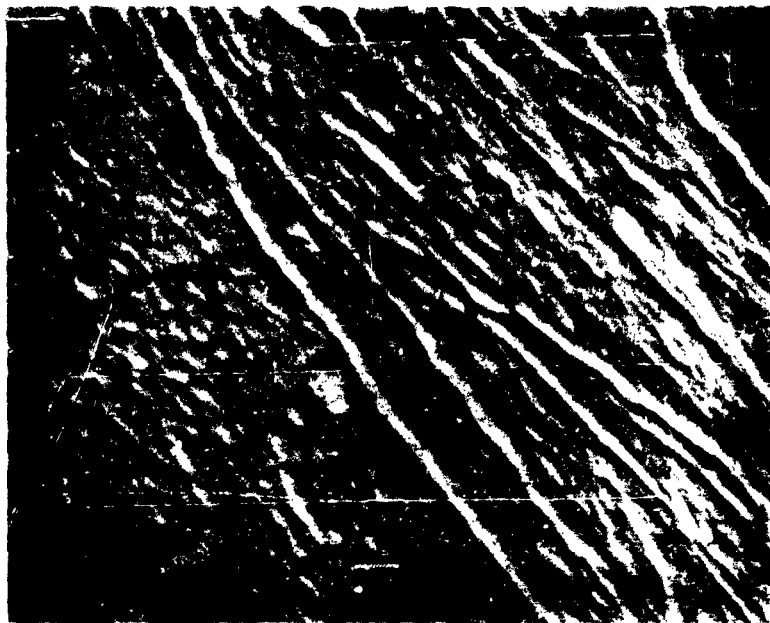
Figure 38. Hy-Tuf, 275,000 psi, Surface Replica, 27,000 X
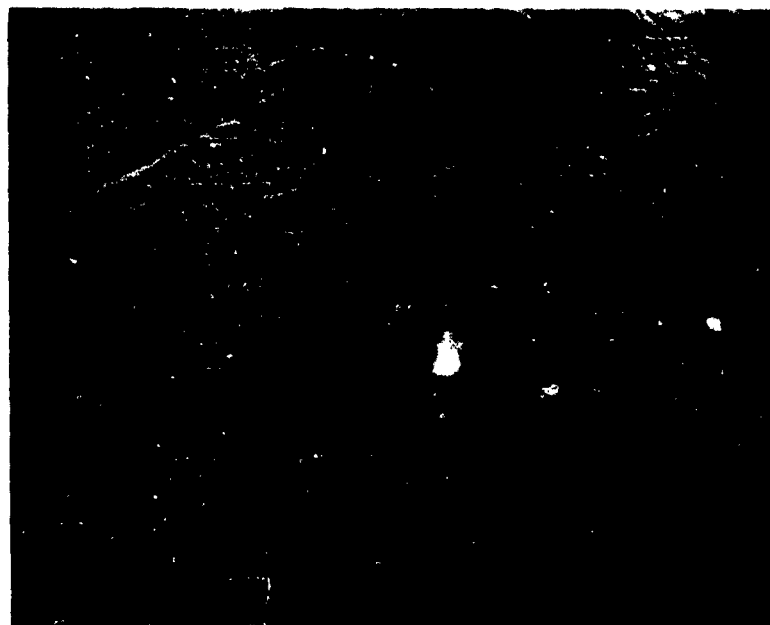Extended Carbide Films and Smaller Particles

Figure 39. Hy-Tuf, 250,000 psi, Surface Replica, 14,000 X
General Microstructure, Raised Areas Possibly
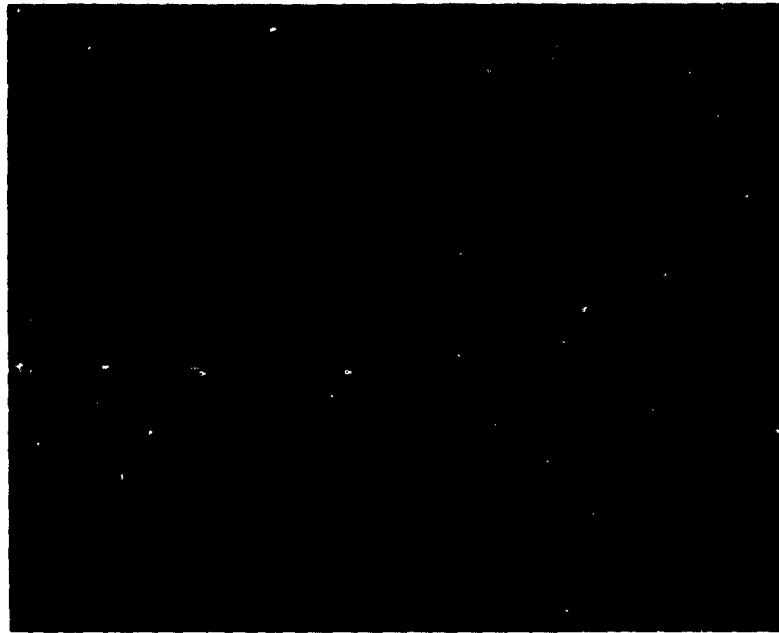Indicative of Retained Austenite

Figure 40. Hy-Tuf, 250,000 psi, Surface Replica, 27,000 X
High Magnification View of Microstructure

Figure 41. 300M, 275,000 psi, Extraction Replica, 21,000 X
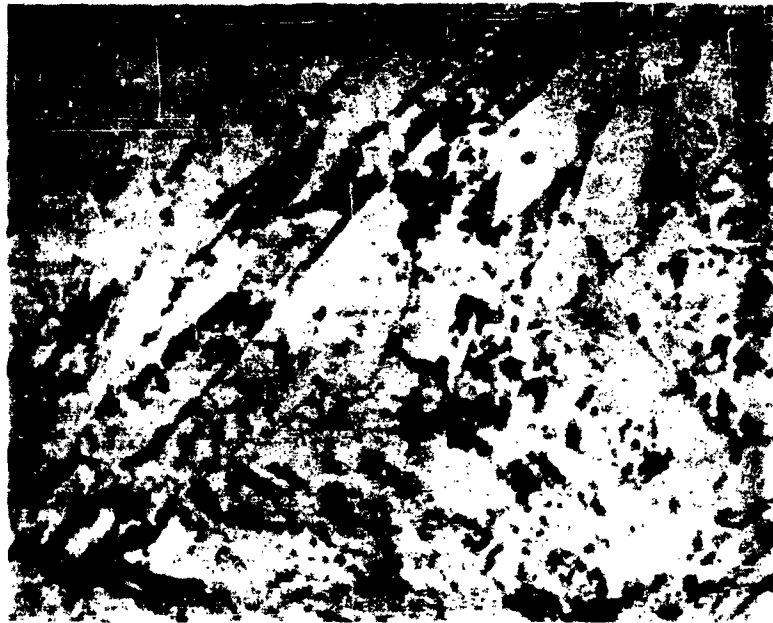General Microstructure

65

Figure 42. 300M, 275,000 psi, Extraction Replica, 35,000 X
High Magnification View of Microstructure
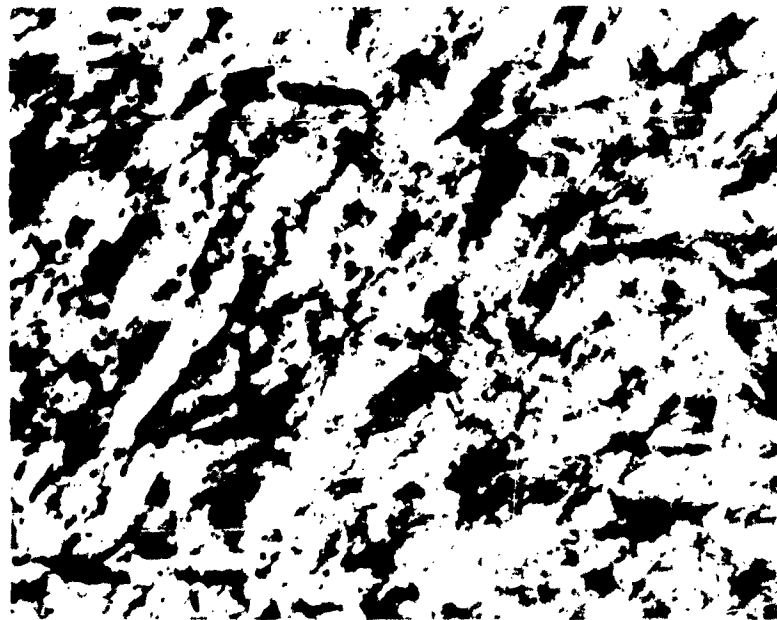
Figure 43. 300M, 250,000 psi, Extraction Replica, 14,000 X
General Microstructure, Precipitation Concentrated
in certain Areas and Sparse in Others is Seen.

Figure 42. 300M, 275,000 psi, Extraction Replica, 35,000 X
High Magnification View of Microstructure

Figure 43. 300M, 250,000 psi, Extraction Replica, 14,000 X
General Microstructure, Precipitation Concentrated
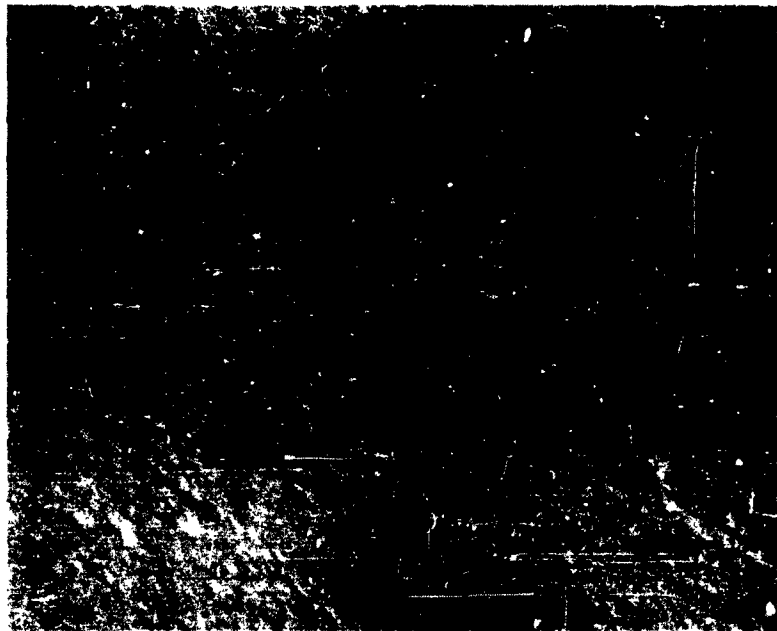in certain Areas and Sparse in Others is Seen.

Figure 44. 300M, 250,000 psi, Surface Replica, 27,000 X
Areas Bare of Carbides are Seen

The heat treatments used to produce the two strength levels in 300M are such that "500°F embrittlement" should result (30). Moreover, the presence of silicon has been found to increase the severity of this embrittlement when it ensues (31). However, those criteria of morphology, such as coarse elongated or parallel cementite platelets and cementite precipitated semi-continuously at martensite plate boundaries and former austenite grain boundaries, which were thought to signal this embrittlement, are very little in evidence. The carbides are, on the whole, appreciably less coarse than in the preceding steels. Therefore, it is proposed that the embrittlement in this steel may be due, at least partially, to the relatively large areas of ferrite free of carbides which were observed in the figures. These areas, surrounded by higher strength material containing dispersed carbides, would be likely areas for the nucleation of cracks. Plastic flow will be restricted due to the stronger material surrounding these bare areas, and the low cohesive strength of ferrite might well permit the formation of a crack. Moreover, if a crack is nucleated at some other discontinuity, such as an inclusion, it will be furnished an easy path for extended growth through these carbide-free paths of ferrite.

5. MX-2 (single and double VAM)

No differences were found between the microstructures of the single- and double-vacuum melted steels. Figures 45 and 46 depict the microstructures developed at the 275,000 psi strength level. Electron diffraction analysis revealed only ϵ-carbide at this strength level. Figures 47 and 48 deal with the lower strength level. Areas of ferrite bare of carbides, and platelet cementite are seen. Electron diffraction analysis revealed primarily Fe_3C at this strength level.

The developer of this steel (Mellon Institute) reports that a slight embrittlement ensues upon tempering MX-2 at 700°F and somewhat above (32). It is interesting, therefore, to consider Figure 49 which deals with this steel tempered at 735°F. Large cementite particles, as well as semi-continuous platelets in former austenite grain boundaries are seen. This experimental steel at 250,000 psi was tempered at 680°F and as can be seen in Figures 47 and 48 platelet cementite and bare areas of ferrite are present. Therefore, MX-2 might be expected to be somewhat embrittled at the lower strength level. Again the extent of this embrittlement cannot be predicted, particularly due to the lack of understanding of the entire effect of the high (1%) cobalt content of MX-2.

6. H-11 (air and vacuum melted)

Again no differentiation between the air- and vacuum-melted steels could be made. Moreover, little difference was seen between H-11 at the two strength levels studied. The possible presence of certain alloy carbides as well as Fe_3C was indicated by electron diffraction. Figures 50 through 52 show the various carbides present at 275,000 psi. Electron diffraction analysis of the area of Figure 50, which depects large alloy carbides, yielded a pattern that appeared to be predominantly $M_{23}C_6$. Fine Widmanstätten and more
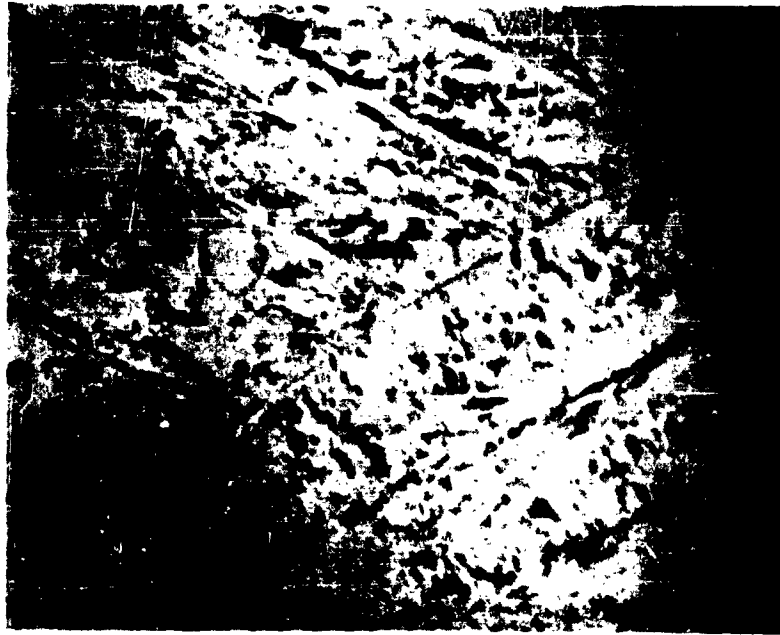
Figure 45. MX-2 (double melted), 275,000 psi, Extraction Replica, 24,000 X
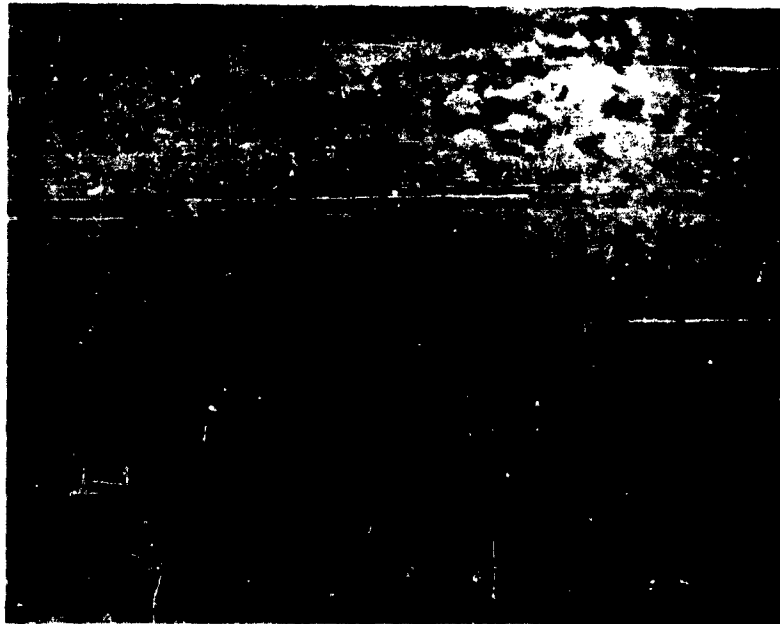High Magnification Shot of a General Nature

Figure 46. MX-2 (double melted), 275,000 psi, Extraction Replica, 35,000 X
Detailed View of Precipitation Within and About a Martensite Plate

Figure 47. MX-2 (double melted), 250,000 psi, Surface Replica, 35,000 X
Area Bare of Carbides is Seen

Figure 48. MX-2 (double melted), 250,000 psi, Extrac'__un Replica, 35,000 X
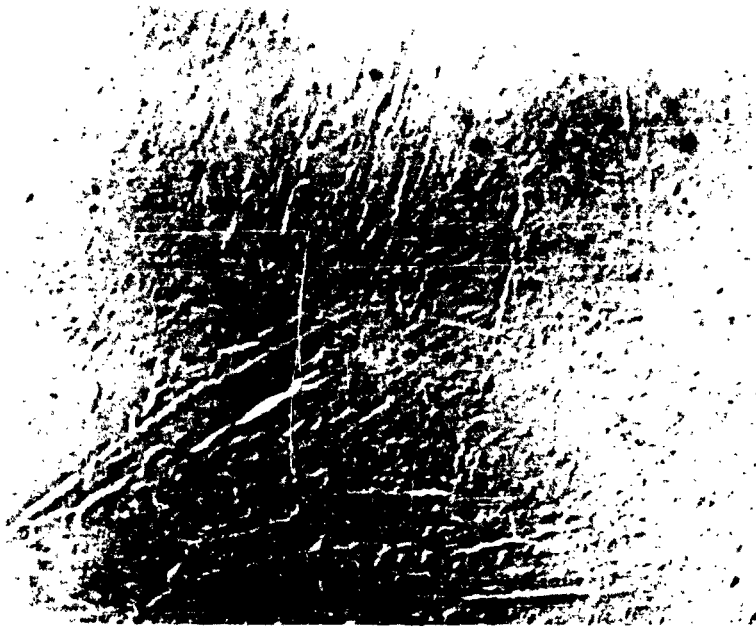Platelet Cementite

Figure 49. MX-2 (single melted), Tempered at 735°F, Surface Replica, 14,000 X
Semi-Continuous Grain Boundary Precipitation

Figure 50. H-11 (air), 275,000 psi, Extraction Replica, 14,000 X
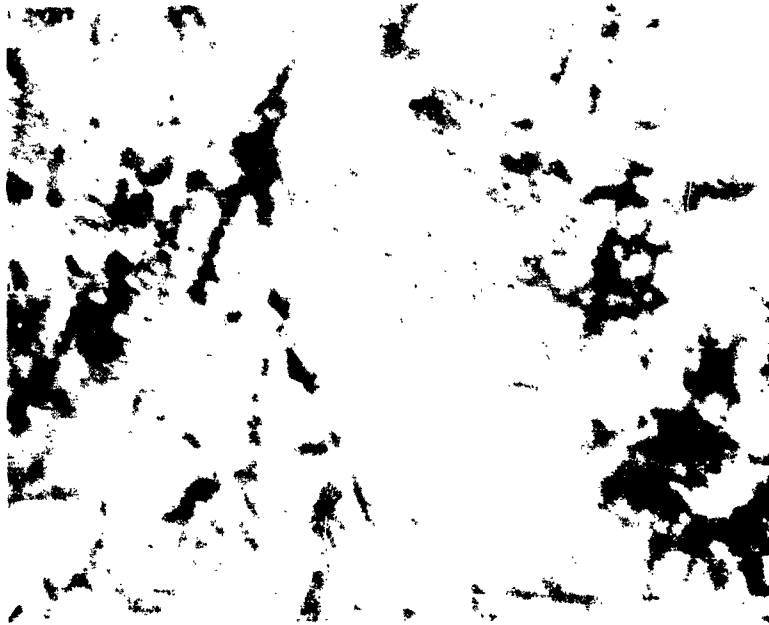Large Alloy Carbides in Evidence

Figure 51. H-11 (air), 275,000 psi, Extraction Replica, 35,000 X
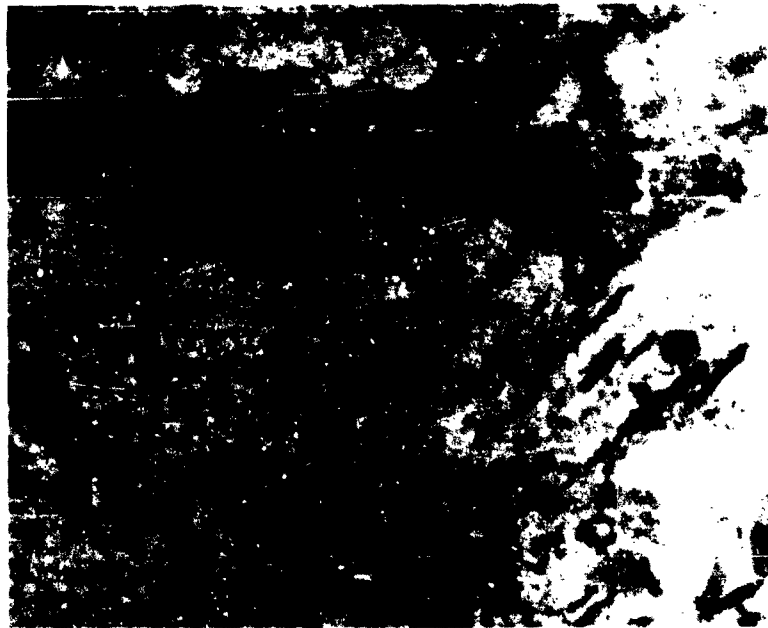Fine Widmanstätten Precipitates Are in Evidence

Figure 52. H-11 (vac.), 275,000 psi, Extraction Replica, 50,000 X
Very Fine and Larger, Rounded Carbides

rounded carbides, as well as the larger carbides, are seen in the other figures. Figures 53, 54, and 55 deal with the lower strength level. Again various types of carbides are seen. Electron diffraction analysis of areas such as deputed in Figure 54 revealed Fe_3C and possibly MC.

The onset of secondary hardening for H-11 has been reported to occur at about 950°F (28). Recent research (33) has suggested that this secondary hardening may be associated with the precipitation of numerous small alloy carbides. In the same research, the large platelet precipitates observed were reported to be predominant at lower tempering temperatures. Therefore, indications are that these steels at the experimental strength levels are in the early stages of secondary hardening. Moreover, this steel tested in sheet form has exhibited very low ductility when tempered between 900° and 1000°F (34). The ductility of this steel might, therefore, be somewhat empaired at the two strength levels studied. Whether this embrittlement is due to the microstructural features seen, or is the result of different phenomena, cannot be predicted at this state of understanding.

D. SUMMARY

The microstructural examination of these steels is summarized in Table XI. AISI 4340, D6, and D6AC have coarser carbides than 300M and MX-2. D6 and D6AC also contain undissolved carbides. However, all have features of morphology, such as platelet precipitates, parallel platelet colonies and areas of ferrite bare of carbides, felt to be detrimental. Moreover, they appear to have been tempered in the range where third stage tempering begins, bringing with it "500°F embrittlement." Hy-Tuf would be expected to have the limited ductility of lightly tempered steels; however, its low carbon content and freedom from "500°F embrittlement" are in its favor. H-11 can be expected to be somewhat embrittled. As a result of secondary hardening, the extent of the embrittlement and its relative effect, however, are unknown.
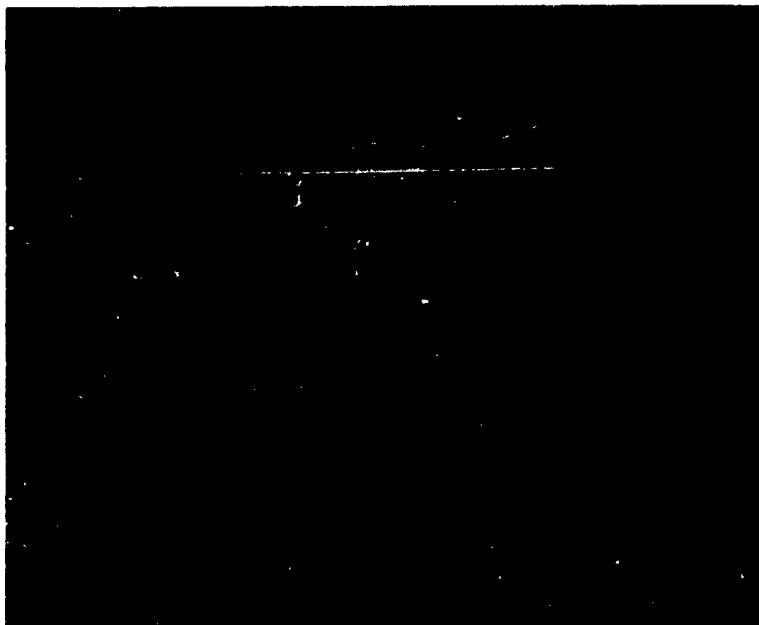
Figure 53.   H-11 (vac.), 250,000 psi, Surface Replica, 14,000 X
             Extended Carbides and Parallel Carbides

Figure 54.   H-11 (vac.), 250,000 psi, Surface Replica, 35,000 X
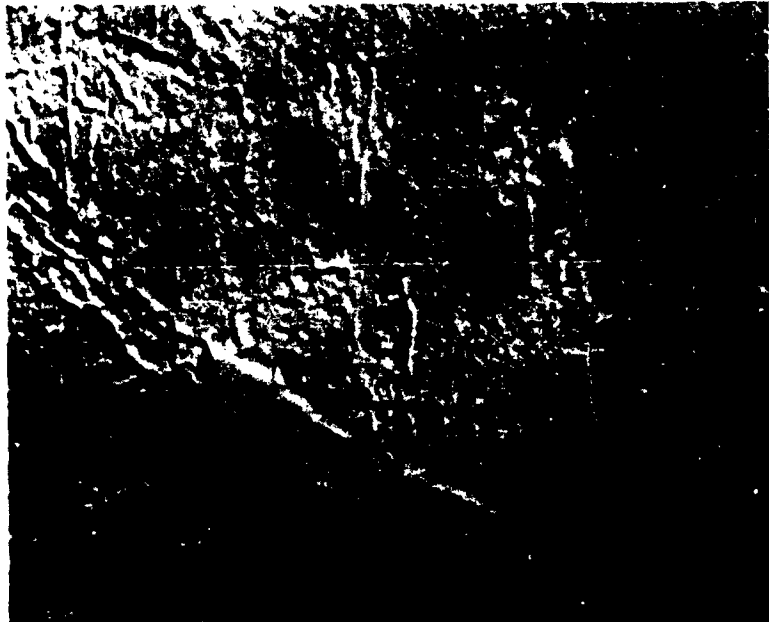   Fine Structure Illustrated

Figure 55. H-11 (vac.), 250,000 psi, Surface Replica, 35,000 X
Grain Boundary Precipitation

Table XI. Summary of Microstructures

Steel	Carbide Composition				Carbide Morphology				
275,000 psi / 250,000 psi	ε	Fe$_3$C	Alloy	Undissolved	Coarse	Fine	Films	Platelets	Bare Areas
AISI 4340			unobserved / unobserved				few / unobs.	few / many, parallel	unobserved / unobserved
D6A and D6AC			unobs. / unobs.	some / some					
Hy-Tuf			unobserved / unobserved				few / few	few / many, parallel	unobserved / unobserved
300M			unobserved / unobserved				many / some	unobs. / unobs.	unobserved / unobserved
MX-2			unobserved / unobserved				few / few	unobs. / unobs.	few / some
H-11			unobserved / unobserved				some / few	unobs. / some	few / few
			unobserved / unobserved		Very Mixed Microstructure Displaying All Morphologies				unobserved / unobserved

† Indicates limited certainty

*

76

REFERENCES

(1) American Society for Metals, Metals Handbook, 1948 ed., p. 88.

(2) Nadai, A., "Theory of Flow and Fracture of Solids," McGraw-Hill Book Company, Inc., 1950, p. 70.

(3) Dieter Jr., G. E., "Mechanical Metallurgy," McGraw-Hill Book Company, Inc., 1961, p. 247.

(4) Marin, J., "Mechanical Behavior of Engineering Materials," Prentice-Hall, Inc., 1962, p. 33.

(5) Low, J. R., and Garafalo, F., "Precision Determination of Stress-Strain Curves in the Plastic Range," Proc. Soc. Experimental Stress Analysis, Vol. 4, No. 2, 1947, pp. 16-25.

(6) Marin, J., "Mechanical Behavior of Engineering Materials," Prentice-Hall, Inc., 1962, p. 39.

(7) Young, A. P. and Marsh, L. L., "A Method for Observing the Progress of Deformation in Tensile Samples," Trans. AIME. 212, 1958, pp. 247-249.

(8) Mason, W., "The Lüders' Lines on Mild Steel," Proc. of Phy. Soc., Vol. 23, 1910-11, pp. 305-333.

(9) Nadai, A., "Theory of Flow and Fracture of Solid," McGraw-Hill Book Company, Inc., 1950, pp. 275-278.

(10) Polakowski, N. H., and Mostovoy, S., "Transient and Destructive Instability in Torsion," Trans. ASM, Vol. 54, No. 3, 1961, pp. 567-578.

(11) Nadai, A., "Theory of Flow and Fracture of Solid," McGraw-Hill Book Company, Inc., 1950, pp. 347-349.

(12) Work, C. E. and Dolan, T. J., "The Influence of Strain and Temperature on the Strength and Ductility of Mild Steel in Torsion," Proc., ASTM, Vol. 53, 1953, p. 626.

(13) Bridgman, P. W., "The Stress Distribution at the Neck of a Tension Specimen," Trans. ASM, Vol. 32, 1944, p. 553.

(14) Nadai, A., "Theory of Flow and Fracture of Solid," McGraw-Hill Book Company, Inc., Vol. 1, 1950, p. 316.

(15) Ross, S. T., Sernka, R. P., and Jominy, W. E., "Some Relationships between Endurance Limit and Torsional Properties of Steel," Trans ASM, Vol. 48, 1956, pp. 119-148.

(16) Gensamer, M., "Strength of Metals under Combined Stresses," ASM, Cleveland, 1940, p. 16.

(17) Shimelevich, I. L., "Concerning Static Bend Tests of Notched Specimens,' Collection of works on mechanical testing (Russian), publisher unknown.

(18) Mott, N. F., Lecture at the Strength of Solids Symposium, Bristol Univ., 1948.

(19) Komarnitsky, R. S., "Liquid Carburizing," Metal Progress, 50, (1946), pp. 665-669.

(20) Wells, A. A., "The Geometrical Site Effect in Notch Brittle Fracture," Trans. of the N. E. Coast Inst. of Engineers and Shipbuilders, 71, (1955), pp. 277-290.

(21) Winne, D. H. and Wundt, B. M., "Application of the Griffith-Irwin Theory of Crack Propagation to the Bursting Behavior of Disks, Including Analytical and Experimental Studies," A.S.M.E. Paper No. 57-A-249, 23 pp.

(22) Spretnak, J. W., The Relationship of Microstructure to Strength and Toughness in High Strength Steels, Fifth Quarterly Progress Report, Contract No. AF 33(616)-7780, ASD, 1 April 1962 - 30 June 1962.

(23) Cahn, J. W. and J. Nutting, "Transmission Quantitative Metallography," Trans. AIME 215 (1959), pp. 526-528.

(24) Hilliard, J. E., "Volume Fraction Analysis by Quantitative Metallography," General Elec. Research Lab. Report No. 61-RL-2652M (March, 1961), 33 pp.

(25) Klinger, L. J., Barnett, N. J., Frohmberg, R. P., and A. R. Troiano, "The Embrittlement of Alloy Steels at High Strength Levels," Trans. ASM, 46, (1954), pp. 1557-1589.

(26) Lement, B. S., Averbach, B. L., and M. Cohen, "Microstructural Changes on Tempering Iron Carbon Alloys," Trans. ASM, 46, (1954), pp. 851-877.

(27) Capus, J. M., "The Influence of Trace Elements Upon the Impact Resistance of Hardened and Tempered Low Alloy Steels," Revue de Metallurgie, August-September 1959, pp. 184-189.

(28) Vasco Jet 1000. Latrobe, Pa.: Variadium Alloys Steel Co. (1959), 25 pp.

(29) ManLabs, Inc., Metallurgical Variables Affecting Fracture Toughness in in High Strength Sheet Alloys, Progress Report No. 3, Contract No. AF 33(616)-8155, ASD, Dec. 31, 1961.

(30) 300M Ultra High Strength Steel. New York: The International Nickel Co., Inc. (1959), 12 pp.

(31) Alstetter, C. J., Cohen, M., and B. L. Averbach, "Effect of Silicon on the Tempering of AISI 43XX Steels," Trans. ASM 55 (June 1962), pp. 287-299.

(32) MX-2 Ultra-High Strength Steel for High Performance Solid Propellant Missile Motor Applications. Pittsburgh, Pa.: The Mellon Institute (1961), 49 pp.

(33) Banerjee, B. R., and J. J. Hauser, Research and Application Engineering
      to Determine the Effects of Processing Variables on Crack Propagation
      in High Strength Steels and Titanium, Fourth Quarterly Progress Report,
      Contract No. AF 33(616)-8156, ASD, May 1, 1962.

(34) ManLabs, Inc., Metallurgical Variables Affecting Fracture Toughness in
      High Strength Sheet Alloys, Progress Report No. 4, Contract No.
      AF 33(616)-8155, ASD, April 1, 1962.

1. High strength steels
I. AFSC Project 7351, Task 735105
II. Contract No. AF 33(616)-7780
III. Ohio State University, Columbus, O.
IV. Y. H. Liu et al
V. Not avail fr OTS
VI. In ASTIA collection

Aeronautical Systems Division, Dir/Materials and Processes, Metals and Ceramics Lab., Wright-Patterson AFB, Ohio.
Rpt No. ASD-TDR-62-1064. THE RELATIONSHIP OF MICROSTRUCTURE TO STRENGTH AND TOUGHNESS IN HIGH STRENGTH STEEL. Final report, Apr 63, 79 pp. incl illus., tables, 34 refs.
Unclassified Report

This research deals with the relationship between the microstructural features and the susceptibility to brittle fracture of six selected commercially produced ultra-high strength steels. The parameters selected for the susceptibility to brittle fracture were the susceptibility to plastic insta-
(over)

bility, indicative of the susceptibility to ductile fracture initiation, and controlled total available energy bend test to determine the conditions for acceleration of crack propagation and the energy absorbed in rapid crack propagation. The microstructures were studied by standard techniques of optical microscopy, electron microscopy, and electron diffraction.